

1 **A Regional multi-Air Pollutant Assimilation System (RAPAS v1.0)**
2 **for emission estimates: System development and application**

3 Shuzhuang Feng¹, Fei Jiang^{1,2}, Zheng Wu³, Hengmao Wang^{1,2}, Wei He¹, Yang Shen¹,
4 Lingyu Zhang¹, Yanhua Zheng¹, Chenxi Lou¹, Ziqiang Jiang⁴, Weimin Ju^{1,2}

5
6 ¹ *Jiangsu Provincial Key Laboratory of Geographic Information Science and Technology, International*
7 *Institute for Earth System Science, Nanjing University, Nanjing, 210023, China*

8 ² *Jiangsu Center for Collaborative Innovation in Geographical Information Resource Development and*
9 *Application, Nanjing, 210023, China*

10 ³ *Chongqing Institute of Meteorological Sciences, Chongqing, 401147, China*

11 ⁴ *Jiangsu Environmental Monitoring Center, Nanjing, 210019, China*

12
13
14
15
16 *Correspondence to: Fei Jiang (jiangf@nju.edu.cn)*

30 **Abstract**

31 Top-down atmospheric inversion infers surface-atmosphere fluxes from spatially
32 distributed observations of atmospheric compositions, which is a vital means for
33 quantifying anthropogenic and natural emissions. In this study, we developed a
34 Regional multi-Air Pollutant Assimilation System (RAPAS v1.0) based on the Weather
35 Research and Forecasting/Community Multiscale Air Quality Modelling System
36 (WRF/CMAQ) model, the three-dimensional variational (3DVAR) algorithm, and the
37 ensemble square root filter (EnSRF) algorithm. This system can simultaneously
38 assimilate hourly *in situ* CO, SO₂, NO₂, PM_{2.5} and PM₁₀ observations to infer gridded
39 emissions of CO, SO₂, NO_x, primary PM_{2.5} (PPM_{2.5}), and coarse PM₁₀ (PMC) on a
40 regional scale. In each data assimilation window, we use a “two-step” scheme, in which
41 the emission is inferred first, and then input into the CMAQ model to simulate initial
42 condition (IC) of the next window. The posterior emission is transferred to the next
43 window as the prior emission, and the original emission inventory is only used in the
44 first window. Additionally, a “super-observation” approach is implemented to decrease
45 the computational costs, observation error correlations, and influence of representative
46 errors. Using this system, we estimated the emissions of CO, SO₂, NO_x, PPM_{2.5}, and
47 PMC in December and July 2016 over China using nationwide surface observations.
48 The results showed that compared to the prior emissions (MEIC 2016), the posterior
49 emissions of CO, SO₂, NO_x, PPM_{2.5}, and PMC in December 2016 increased by 129%,
50 20%, 5%, 95%, and 1045%, respectively, and the emission uncertainties decreased by
51 44%, 45%, 34%, 52%, and 56%, respectively. With the inverted emissions, the RMSE
52 of simulated concentrations decreased by 40–56%. Sensitivity tests were conducted
53 with different ~~inversion processes~~, prior emissions, prior uncertainties, and observation
54 errors. The results showed that the “two-step” scheme employed in RAPAS is robust in
55 estimating emissions using nationwide surface observations over China. This study
56 offers a useful tool for accurately quantifying multi-species anthropogenic emissions at
57 large scales and in near real time.

58

59 **1. Introduction**

60 Owing to rapid economic development and pollution control legislation, there is an
61 increasing demand to provide updated emission estimates, especially in areas where
62 anthropogenic emissions are intensive. Accurately estimating source emission
63 quantities and spatiotemporal changes resulting from various regulations is imperative
64 and valuable for understanding air quality responses and is crucial for providing timely
65 instructions for the design of future emission regulations. However, most inventories
66 were developed based on a bottom-up approach and are usually updated with a delay
67 of a few years owing to the complexity of gathering statistical information on activity
68 levels and sector-specific emission factors (Ding et al., 2015). The large uncertainty
69 associated with the low temporal and spatial resolutions of these datasets also greatly
70 limits the assessment of emission changes. Some studies (Bauwens et al., 2020; Shi and
71 Brasseur, 2020) evaluated emission changes indirectly through concentration
72 measurements; however, air pollution changes are not only dominated by emission
73 changes, but also highly affected by meteorological conditions (Shen et al., 2021).

74 Top-down atmospheric inversion infers surface-atmosphere fluxes from spatially
75 distributed observations of atmospheric compositions. Recent efforts have focused on
76 developing air pollution data assimilation (DA) systems to conduct top-down
77 inversions, which can integrate model and multi-source observational information to
78 constrain emission sources. Two major methods are widely used in those DA systems:
79 4D-variational data assimilation (4DVAR) and ensemble Kalman filter (EnKF).
80 4DVAR provides a global optimal analysis by minimizing a cost function. It shows an
81 implicit flow-dependent background error covariance and can reflect complex
82 nonlinear constraint relationships (Lorenc, 2003). Additionally, a weak constraint
83 4DVAR method can partly account for the model error by defining a systematic error
84 term in a cost function (Derber, 1989). For example, the GEOS-Chem and TM5 4DVAR
85 frameworks have been used to estimate CH₄ (Alexe et al., 2015; Monteil et al., 2013;
86 Schneising et al., 2009; Stanevich et al., 2021; Wecht et al., 2014) and CO₂ fluxes (Basu
87 et al., 2013; Nassar et al., 2011; Wang et al., 2019a) from different satellite retrieval

88 products. Additionally, Jiang et al. (2017) and Stavrou et al. (2008) also used the
89 4DVAR algorithm to estimate global CO and NO_x emission trends using MOPITT and
90 GOME/SCIAMACHY retrievals, respectively. Using NIES LiDAR observations,
91 Yumimoto et al. (2008) applied the 4DVAR DA to infer dust emissions over eastern
92 Asia and the results agreed well with various satellite data and surface observations.
93 Based on surface observations, Meirink et al. (2008) developed a 4DVAR system to
94 optimize monthly methane emissions, which showed a high degree of consistency in
95 posterior emissions and uncertainties when compared with an analogous inversion
96 based on the traditional synthesis approach.

97 Although considerable progress has been made to reduce large uncertainties in emission
98 inventories, the drawback of the 4DVAR method is the additional development of
99 adjoint models, which are technically difficult and cumbersome for complex chemical
100 transport models (Bocquet and Sakov, 2013). Instead, EnKF uses flow-dependent
101 background error covariance generated by ensemble simulations to map deviations in
102 concentrations to increments of emissions, which is more flexible and easier to
103 implement. Many previous studies used EnKF techniques to assimilate single- or dual-
104 species observations to optimize the corresponding emission species (Chen et al., 2019;
105 Peng et al., 2017; Schwartz et al., 2014; Sekiyama et al., 2010). Miyazaki et al. (2017)
106 improved NO_x emission estimates using multi-constituent satellite observations, and
107 further estimated global surface NO_x emissions from 2005 to 2014. Feng et al., (2020b)
108 used surface observations of NO₂ to infer the NO_x emission changes in China during
109 the COVID-19, and quantitatively evaluate the impact of the epidemic on economic
110 activities from the perspective of emission change. Tang et al. (2011) adjusted the
111 emissions of NO_x and VOCs through assimilating surface O₃ observations and achieved
112 an better performance in O₃ forecasts. However, such a revision may encounter the
113 problem of model error compensation rather than a retrieval of physically meaningful
114 quantities, which should be avoided from overfitting for emission inversion purposes
115 (Bocquet, 2012; Navon, 1998; Tang et al., 2011). The EnKF has also been widely
116 applied to optimize emissions of carbon dioxide (Jiang et al., 2021; Liu et al., 2019),

117 carbon monoxide (Feng et al., 2020a; Mizzi et al., 2018), sulfur dioxide (Chen et al.,
118 2019), ammonia (Kong et al., 2019), etc.

119 Multi-species data assimilation can efficiently reduce the uncertainty in emission
120 inventories and has led to improvements in air quality forecasting (Ma et al., 2019;
121 Miyazaki et al., 2012b) as it offers additional constraints on emission estimates through
122 improvements in related atmospheric fields, chemical reactions, and gas-particle
123 transformations (Miyazaki and Eskes, 2013). Barbu et al. (2009) updated sulfur oxide
124 (SO_x) emissions with SO_2 and sulfate aerosol observations and found that the
125 simultaneous assimilation of both species performed better than assimilating them
126 separately. Muller and Stavrou (2005) also found that the simultaneous optimization
127 of the sources of CO and NO_x led to better agreement between simulations and
128 observations compared to the case where only CO observations are used.

129 The deviation in the chemical initial condition (IC) is an important source of error that
130 affects the accuracy of emission inversion because atmospheric inversion fully
131 attributes the biases in simulated and observed concentrations to deviations in
132 emissions (Meirink et al., 2006; Peylin et al., 2005). The biases of concentrations would
133 be compensated by the unreasonable adjustment of pollution emissions without the
134 optimization of ICs (Tang et al., 2013). Simultaneously optimizing chemical ICs and
135 emissions has been applied to constrain emissions in many previous studies (Ma et al.,
136 2019; Miyazaki et al., 2012a; Peng et al., 2018). For example, Elbern et al. (2007)
137 adjusted O_3 ICs, NO_x ICs and emissions, VOCs ICs and emissions jointly through
138 assimilating surface O_3 and NO_x observations. Although the forecast skills of O_3 were
139 improved, due to the coarse model resolution and the strong nonlinear relationship
140 between O_3 and NO_x , the assimilation of O_3 observation worsened emission inversion
141 and forecast of NO_x . Peng et al. (2018) assimilated near-surface observations to
142 simultaneously optimize the ICs and emissions. In the 72-hr forecast evaluation, their
143 resultant emission succeeded in improving SO_2 forecast while having little influence
144 on CO and aerosol forecast and even degrading the forecast of NO_2 . Ma et al. (2019)
145 also found that the DA benefits for forecast almost disappeared after 72 hr using

146 optimized ICs and emissions. Although a large improvement has been achieved, this
147 method has significant limitations in emission inversion as the contributions from the
148 emissions and chemical ICs to the model's biases are difficult to distinguish (Jiang et
149 al., 2017). In addition, the constraints of the chemical ICs with observations in each
150 assimilation window make the emission inversions between the windows independent.
151 This means that if the emission in one window is overestimated or underestimated, it
152 cannot be transferred to the next window for further correction and compensation.
153 Considering the importance of emissions in chemical field prediction (Bocquet et al.,
154 2015), the rapid disappearance of the DA benefits seems unrealistic, indicating that
155 simultaneously optimizing chemical ICs and emissions may result in a systematic bias
156 in the inverted emissions (Jiang et al., 2021).

157 Since 2013, China has deployed an air pollution monitoring network that publishes
158 nationwide and real-time hourly surface observations. This dataset provides an
159 opportunity to improve emission estimates using the DA. In this study, a regional multi-
160 air pollutant assimilation system using 3DVAR and EnKF DA techniques was
161 constructed to simultaneously assimilate various surface observations (e.g. CO, SO₂,
162 NO₂, O₃, PM_{2.5}, and PM₁₀). ~~Considering the possible shortcomings of the simultaneous~~
163 ~~optimization method (named “one-step” method in this study), as mentioned by Jiang et~~
164 ~~al. (2021), we~~ adopted a “two-step” method in this system. ~~Unlike the “one-step”~~
165 ~~method, in which~~ the ICs of each DA window ~~in the “two-step” method~~ were simulated
166 using the posterior emissions of the previous DA window. The capabilities of RAPAS
167 for reanalysis field generation and emission inversion estimation were also evaluated.
168 The robustness of the system was investigated with different prior inventories,
169 uncertainty settings of prior emissions, and observation errors. The remainder of the
170 paper is organized as follows: Section 2 introduces the DA system and observation data,
171 Section 3 describes the experimental design, Section 4 presents and discusses the results
172 of the system performance and sensitivity tests, and Section 5 concludes the paper.

173

174 **2. Method and data**

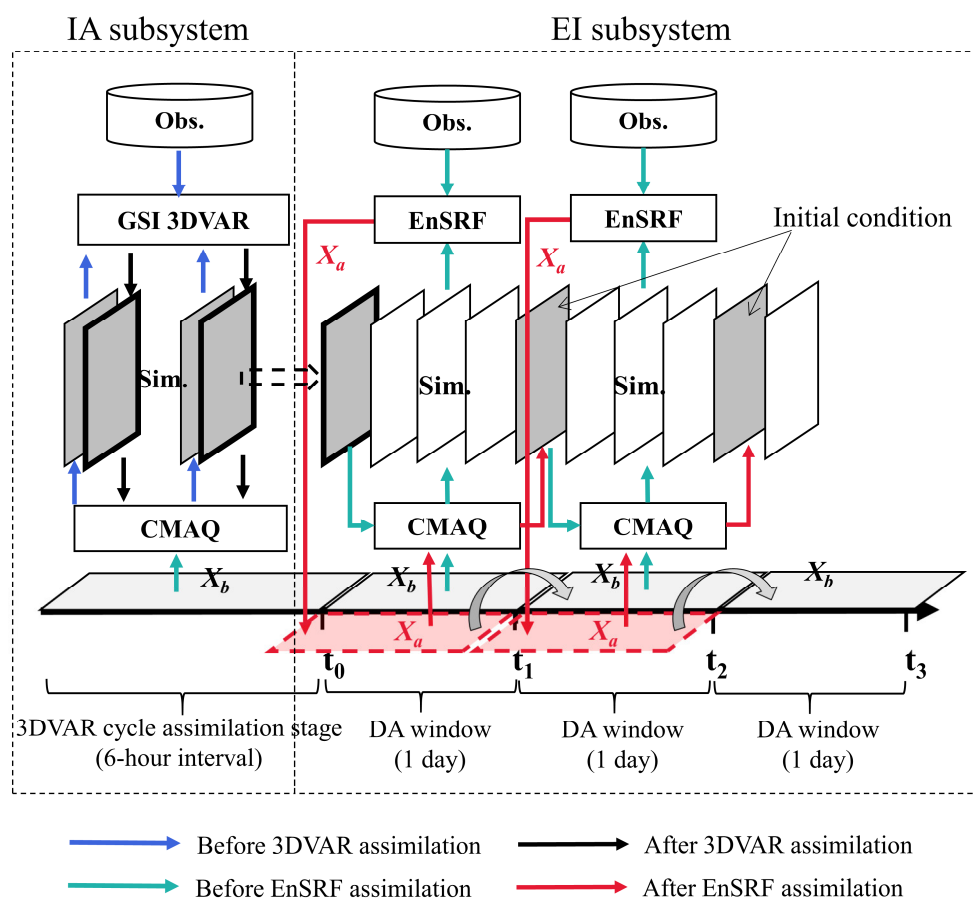
175 **2.1 System description**

176 **2.1.1 Procedure of the assimilation system**

177 A regional air pollutant assimilation system has been preliminarily constructed and
178 successfully applied in our previous studies to optimize the gridded CO and NO_x
179 emissions (Feng et al., 2020a; Feng et al., 2020b). Herein, the system was further
180 extended to simultaneously assimilate multiple species (e.g. CO, SO₂, NO₂, O₃, PM_{2.5},
181 and PM₁₀) and officially named the Regional multi- Air Pollutant Assimilation System
182 (RAPASv1.0). The RAPAS has three components: a regional chemical transport model
183 (CTM), which is coupled offline and used to simulate the meteorological fields and
184 atmospheric compositions, and the 3DVAR and ensemble square root filter (EnSRF)
185 modules, which are used to optimize chemical ICs (Feng et al., 2018; Jiang et al., 2013b)
186 and anthropogenic emissions (Feng et al., 2020a; Feng et al., 2020b), respectively.
187 3DVAR was introduced considering its excellent performance in our previous study and
188 the lower computational cost during the spin-up period in optimizing ICs. Additionally,
189 the 3DVAR method can obtain a better IC than the EnKF method (Schwartz et al., 2014).

190 Based on the above three components, the RAPAS was divided into two subsystems:
191 the IC assimilation (IA) subsystem (CTM plus 3DVAR) and the emission inversion (EI)
192 subsystem (CTM plus EnSRF). As shown in Figure 1, the IA subsystem was first run
193 to optimize the chemical ICs (Kleist et al., 2009; Wu et al., 2002) for the subsequent EI
194 subsystem. Distinguish the source type of model-observation mismatch error was not
195 required for the IA subsystem. The EI subsystem runs cyclically with a “two-step”
196 scheme. In the first step, the prior emissions (\mathbf{X}^b) are perturbed and input into the CTM
197 model to simulate chemical concentration ensembles. The simulated concentrations of
198 the lowest model level were then interpolated to the observation space according to the
199 locations and times of the observations using the nearest-neighbor interpolation method.
200 Prior emissions (\mathbf{X}^b), simulated observations and real observations were entered into
201 the EnSRF module to generate optimized emissions (\mathbf{X}^a). In the second step, the

202 optimized emissions were re-entered into the CTM model to generate the ICs of the
 203 next DA window. Meanwhile, the optimized emissions were transferred to the next
 204 window as prior emissions. Unlike joint adjustment of ICs and emissions (“one-step”
 205 scheme) in emission inversion (Chen et al., 2019)the “one-step” scheme, the “two-step”
 206 scheme needs to run the CTM model twice, which is time consuming but can transfer
 207 the potential errors of the inverted emissions in one DA window to the next for further
 208 correction. ~~The benefits of this scheme are further discussed in Section 4.3.~~



209

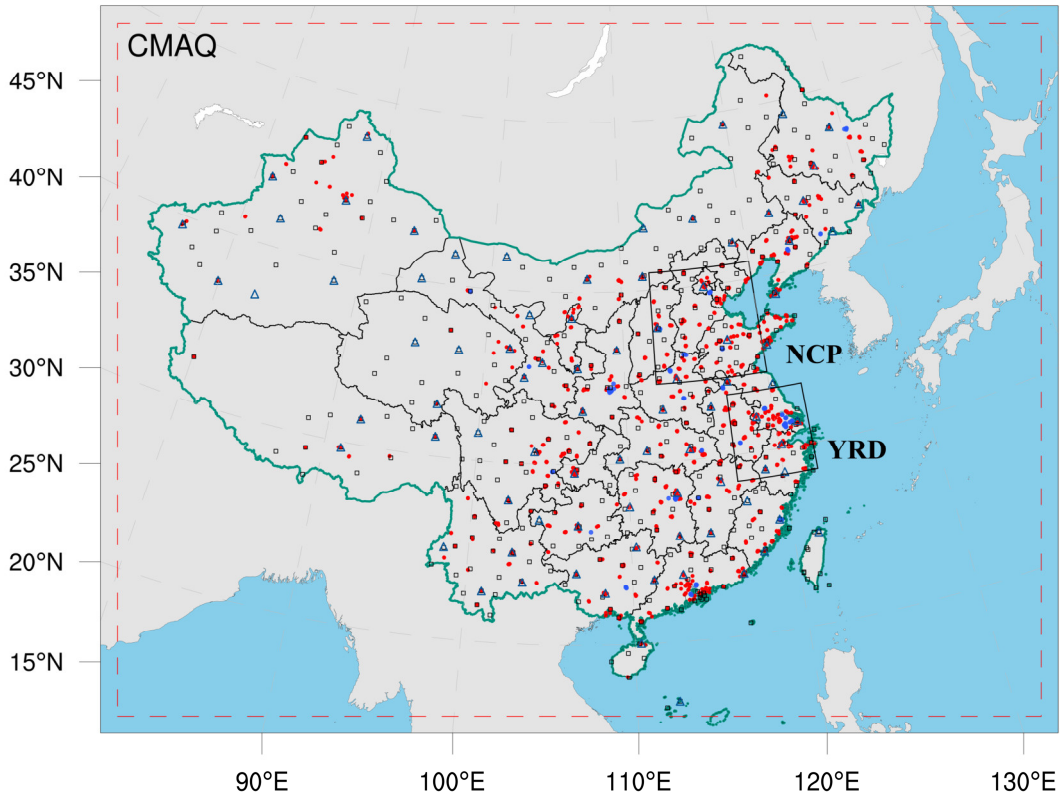
210 **Figure 1.** Composition and flow chart of RAPAS. x_a and x_b represent the prior and
 211 posterior emissions. The 3DVAR assimilation stage lasts five days with data input
 212 frequency of six hours and the DA window in the EI subsystem is set to one day.

213 **2.1.2 Atmospheric transport model**

214 The regional chemical transport model of Weather Research and
 215 Forecasting/Community Multiscale Air Quality Modelling System (WRF/CMAQ) was

216 adopted in this study. CMAQ is a regional 3-D Eulerian atmospheric chemistry and
217 transport model with a “one-atmosphere” design developed by the US Environmental
218 Protection Agency (EPA). It can simultaneously address the complex interactions
219 among multiple pollutants/air quality issues. The CMAQ was driven by the WRF model,
220 which is a state-of-the-art mesoscale numerical weather prediction system designed for
221 both atmospheric research and meteorological field forecasting. In this study, WRF
222 version 4.0 and CMAQ version 5.0.2 were used. The WRF simulations were performed
223 with a 36-km horizontal resolution on 169×129 grids, covering all of mainland China
224 (Figure 2). This spatial resolution has been widely adopted in regional simulations as it
225 can provide good simulations of spatiotemporal variations in air pollutants (Mueller
226 and Mallard, 2011; Sharma et al. 2016). In the vertical direction, there were 51 sigma
227 levels on the sigma-pressure coordinates extending from the surface to 100 hPa. The
228 underlying surface of the urban and built-up land was replaced by the MODIS land
229 cover retrieval of 2016 to adapt to the rapid expansion of urbanization. The CMAQ
230 model was run with the same domain but with three grid cells removed from each side
231 of the WRF domain. There were 15 layers in the CMAQ vertical coordinates, which
232 were interpolated from 51 WRF layers.

233 The meteorological initial and lateral boundary conditions were both provided by the
234 Final Operational Global Analysis data of the National Center for Environmental
235 Prediction (NCEP) with a $1^\circ \times 1^\circ$ resolution at 6-h intervals. The chemical lateral
236 boundary conditions and chemical ICs in the IA subsystem originate from background
237 profiles. As mentioned above, in the EI subsystem, the chemical IC in the first window
238 is provided by the IA subsystem and in the following windows, it is forward simulated
239 using optimized emissions from the previous window. Carbon Bond 05 with updated
240 toluene chemistry (CB05tucl) and the 6th generation aerosol module (AERO6) were
241 chosen as the gas-phase and aerosol chemical mechanisms, respectively (Appel et al.,
242 2013; Sarwar et al., 2012). The detailed physical and chemical configurations are listed
243 in Table 1.



244

245 **Figure 2.** Model domain and observation network. The red dashed frame depicts the
 246 CMAQ computational domain; the black squares represent the surface meteorological
 247 measurement sites; the navy triangles represent the sounding sites; and the red and blue
 248 dots represent the air pollution measurement sites. Observations from all sites were
 249 assimilated in the 3DVAR subsystem, while observations of city sites where red dots
 250 were averaged are used for assimilation and where blue dots were averaged are used
 251 for independent evaluation in the EI subsystem; the boxed subregions are the North
 252 China Plain (NCP) and Yangtze River Delta (YRD); and the shaded area depicts the
 253 topography.

254

255

256

257

258

259 **Table 1.** Configuration options of WRF/CMAQ

| WRF | | CMAQ | |
|----------------|--------------|-------------------------------|-----------------|
| Parameter | Scheme | Parameter | Scheme |
| Microphysics | WSM6 | Horizontal/Vertical advection | yamo/wrf |
| Longwave | RRTM | Horizontal/Vertical diffusion | multiscale/acm2 |
| Shortwave | Goddard | Deposition | m3dry |
| Boundary layer | ACM | Chemistry solver | EBI |
| Cumulus | Kain-Fritsch | Photolysis | phot_inline |
| Land-surface | Noah | Aerosol module | AERO6 |
| Surface layer | Revised | Cloud module | cloud_acm_ae6 |
| Urban canopy | No | Gas-phase chemistry | CB05tucl |

260 **2.1.3 3DVAR assimilation algorithm**

261 Grid-point Statistical Interpolation (GSI) developed by the US NCEP was utilized in
 262 this study. Building on the work of Liu et al. (2011), Jiang et al. (2013b) and Feng et al.
 263 (2018), we extended GSI to simultaneously assimilate multiple species (including CO,
 264 SO₂, NO₂, O₃, PM_{2.5}, and PM₁₀) and first used individual aerosol species of PM_{2.5} as
 265 analysis variables within the GSI/WRF/CMAQ framework. Additional work includes
 266 the construction of surface air pollutant observation operators, the updating of
 267 observation errors, and the statistics of background error covariance for the analysis
 268 variables. Moreover, the data interface was modified to read/write the CMAQ
 269 output/input file directly, which was easy to implement.

270 In the sense of minimum analysis error variance, the 3DVAR algorithm optimizes the
 271 analysis fields with observations by iterative processes to minimize the cost function
 272 ($J(\mathbf{x})$) defined below:

273
$$J(\mathbf{x}) = \frac{1}{2}(\mathbf{x}_a - \mathbf{x}_b)^T \mathbf{B}^{-1}(\mathbf{x}_a - \mathbf{x}_b) + \frac{1}{2}[H(\mathbf{x}_a) - \mathbf{y}]^T \mathbf{R}^{-1}[H(\mathbf{x}_a) - \mathbf{y}], \quad (1)$$

274 where \mathbf{x}_a is a vector of the analysis field, \mathbf{x}_b is the background field, \mathbf{y} is the vector
 275 of observations, \mathbf{B} and \mathbf{R} are the background and observation error covariance matrices,

276 respectively, representing the relative contributions to the analysis, and H is the
277 observation operator that maps the model variables to the observation space.

278 The analysis variables were the 3D mass concentrations of the pollution components
279 (e.g. CO and sulfate) at each grid point. Hourly mean surface pollution observations
280 within a one-hour window of the analysis were assimilated. To assimilate the surface
281 pollution observations, model-simulated compositions were first diagnosed at
282 observation locations. For gas concentrations to be directly used as analysis variables,
283 the units need to be converted from ppm and ppb to mg m^{-3} and $\mu\text{g m}^{-3}$, respectively, to
284 match the observations. The model-simulated $\text{PM}_{2.5}$ and PM_{10} concentrations at the
285 ground level were diagnosed as follows:

$$286 \quad PM_{2.5} = f_i \times PM_i + f_j \times PM_j + f_k \times PM_k = \text{OC} + \text{EC} + \text{SO}_4^{2-} + \text{NO}_3^- + \text{NH}_4^+ + \\ 287 \quad \text{SEAS} + \text{AP}_{2.5} \quad (2)$$

$$288 \quad PM_{10} = PM_i + PM_j + PM_k = PM_{2.5} + \text{PMC} \quad (3)$$

289 where f_i , f_j , and f_k are the $\text{PM}_{2.5}$ fractions of the Aitken, accumulation, and coarse
290 modes, respectively. These ratios are recommended as the concentrations of $\text{PM}_{2.5}$ and
291 fine mode aerosols (i.e. Aitken plus accumulation) can differ because $\text{PM}_{2.5}$ particles
292 include small tails from the coarse mode in the CMAQ model (Binkowski and Roselle,
293 2003; Jiang et al., 2006). PM_i , PM_j , and PM_k are the mass concentrations of the three
294 modes in the CMAQ model, respectively. Seven aerosol species of $\text{PM}_{2.5}$ (organic
295 carbon (OC), elemental carbon (EC), sulfate (SO_4^{2-}), nitrate (NO_3^-), ammonium (NH_4^+),
296 sea salt (SEAS), and fine-mode unspiciated aerosols ($\text{AP}_{2.5}$)) and additional coarse
297 PM_{10} (PMC) were extracted as analysis variables and were updated using the $\text{PM}_{2.5}$ and
298 PMC observations. Before calculating equation (1) within the GSI, the analysis
299 variables were bilinearly interpolated in the horizontal direction to the observation
300 locations.

301 Calculating background error covariance (\mathbf{B}) is generally costly and difficult when a
302 high-dimensional numerical model is used. For simplification, \mathbf{B} was represented as a

303 product of spatial correlation matrices and standard deviations (SDs).

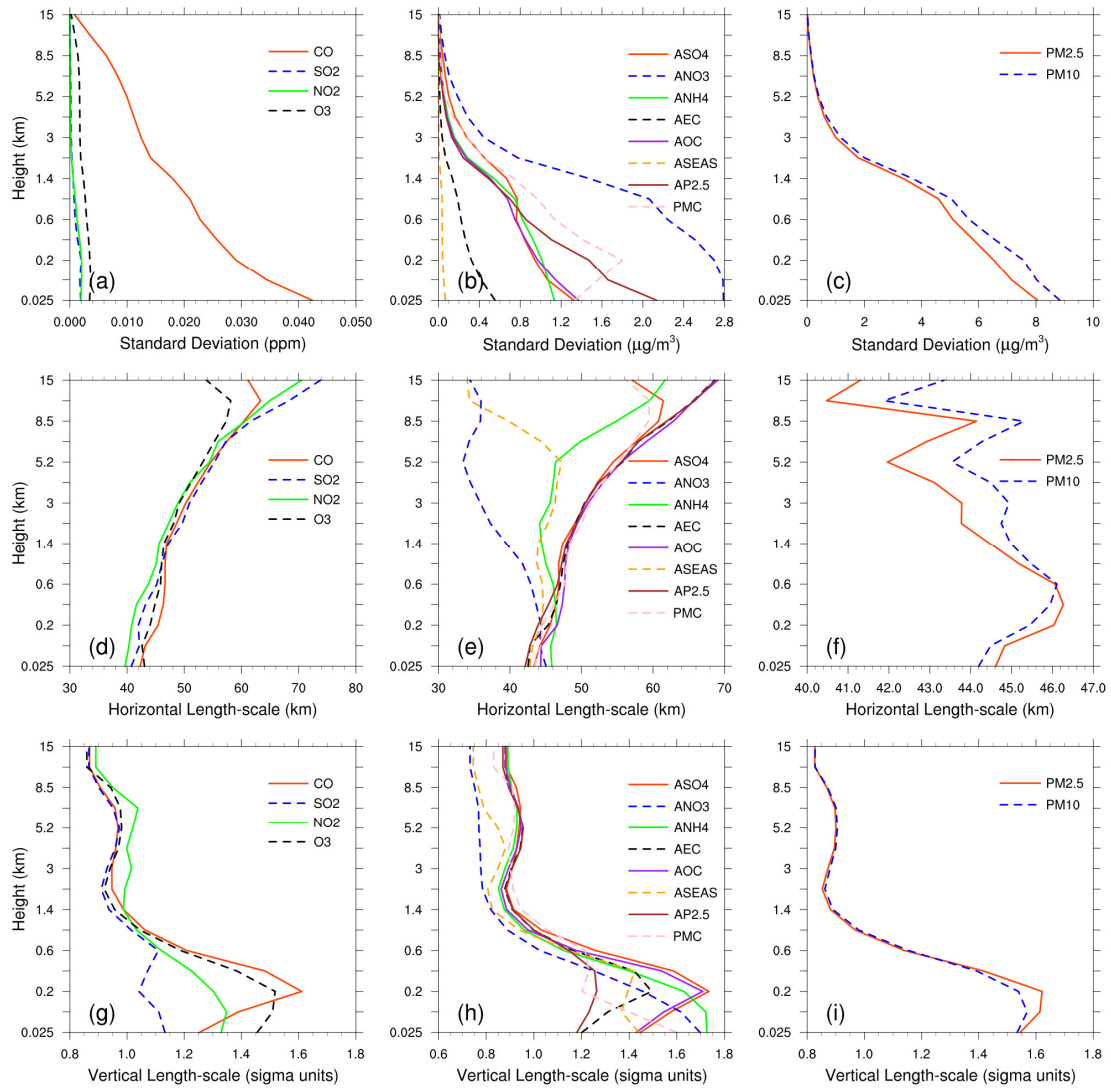
$$304 \quad \mathbf{B} = \mathbf{D}\mathbf{C}\mathbf{D}^T \quad (4)$$

$$305 \quad \mathbf{C} = \mathbf{C}_x \otimes \mathbf{C}_y \otimes \mathbf{C}_z \quad (5)$$

306 where \mathbf{D} is the background error SD matrix; \mathbf{C} is the background error correlation
307 matrix; \otimes is the Kronecker product; and \mathbf{C}_x , \mathbf{C}_y , and \mathbf{C}_z denote three one-
308 dimensional correlation submatrices in the longitude, latitude, and vertical coordinate
309 directions, respectively. \mathbf{C}_x and \mathbf{C}_y are assumed to be horizontally isotropic such that
310 they can be represented using a Gaussian function. The correlation between any two
311 points x_i and x_j in the horizontal direction is expressed as follows:

$$312 \quad c(x_i, x_j) = e^{-\frac{(x_i-x_j)^2}{2L^2}} \quad (6)$$

313 where L is the horizontal correlation scale estimated using the proxy of the
314 background error (Figure 3). The vertical correlation matrix \mathbf{C}_z is directly estimated
315 from the model background field as \mathbf{C}_z is only an $n_z \times n_z$ (here, $n_z=15$) matrix.



316

317 **Figure 3.** Vertical profiles of standard deviations (top, $\mu\text{g m}^{-3}$), horizontal (middle, km)
 318 and vertical (bottom, km) length scales for CO, SO₂, NO₂, O₃, sulfate, nitrate,
 319 ammonium, EC, OC, sea salt, unsciated aerosols (AP_{2.5}), PMC, PM_{2.5} and PM₁₀.

320 To estimate these matrices, the “NMC” method was used to compute **B** for each variable
 321 by taking the differences between forecasts of different lengths valid at the same time
 322 (Parrish and Derber, 1992; Rabier et al., 1998). Differences between the 24- and 12-h
 323 WRF/CMAQ forecasts of 60 pairs (two pairs per day) of analysis variables valid at
 324 either 0000 or 1200 UTC over November 2016 were used. The horizontal and vertical
 325 length scales of the correlation matrices were estimated using recursive filters (Purser
 326 et al., 2003). The vertical distribution of the background error SDs, which varies with
 327 height and species, is shown in Figure 3. The vertical profile of the background error

328 SDs corresponds to the vertical concentration distribution. This means that higher
329 concentrations tend to have larger background error SDs (e.g., CO and nitrate). These
330 SDs exhibit a common reduction as the height increases, especially at the top of the
331 boundary layer. The horizontal correlation of the background error determines the
332 propagation of observation information in this direction, whereas the vertical
333 correlation determines the vertical extension of such increments. For gaseous pollutants
334 and most individual aerosol components, the horizontal length scales increased with
335 height, whereas for the total particulate matter (i.e. PM_{2.5}, PM₁₀), the scales increased
336 with height in the boundary layer and decreased with height in the free troposphere.
337 The ground-level scale generally spread 40–45 km for all control variables. The vertical
338 length scale of most species first increased and then decreased with height, which may
339 be related to vertical mixing (Kahnert, 2008) and stack emissions at approximately 200
340 m height.

341 **2.1.4 EnKF assimilation algorithm**

342 In EnKF, the time-dependent uncertainties of the state variables are estimated using a
343 Monte Carlo approach through an ensemble. Uncertainty can be propagated using linear
344 or nonlinear dynamic models (flow-dependent background error covariance) by simply
345 implementing ensemble simulations. The EnSRF algorithm introduced by Bierman
346 (1977) and Maybeck (1979) was used to constrain pollution emissions in this study.
347 EnSRF is a deterministic EnKF that obviates the need to perturb observations, which
348 has a higher computational efficiency and a better performance (Sun et al., 2009).

349 The perturbation of the prior emissions represents the uncertainty. We implemented
350 additive emission adjustment methods, which were calculated using the following
351 function:

$$352 \quad \mathbf{X}_i^b = \mathbf{X}_0^b + \delta \mathbf{X}_i^b, i = 1, 2, \dots, N \quad (7)$$

353 where \mathbf{b} is the background (prior) state, i is the identifier of the perturbed samples,
354 and N is the ensemble size, which was set to 40 considering the trade-off between
355 computational cost and inversion accuracy (Figure S1). In contrast to the estimation of

356 parameters based on the augmentation of the conventional state vector (e.g.
357 concentrations) with the parameter variables, \mathbf{X} only comprises emissions in this study
358 (similarly hereafter). $\delta\mathbf{X}_i^b$ is the randomly perturbed samples added to the prior
359 emissions \mathbf{X}_0^b to produce ensemble samples of the inputs \mathbf{X}_i^b . $\delta\mathbf{X}_i^b$ is drawn from
360 Gaussian distributions with a mean of zero and standard deviation of the prior emission
361 uncertainty in each grid. The state variables of the emissions include CO, SO₂, NO_x,
362 primary PM_{2.5} (PPM_{2.5}) and PMC. We used variable localization to update the analysis,
363 which means that the covariance among different state variables was not considered,
364 and the emission of one species was constrained only by its corresponding air pollutant
365 observation. This method has been widely used in chemical data assimilation systems
366 to avoid spurious correlations between species (Ma et al., 2019; Miyazaki et al., 2012b).
367 After obtaining an ensemble of state vectors (prior emissions), ensemble runs of the
368 CMAQ model were conducted to propagate the errors in the model with each ensemble
369 sample of state vectors. Combined with the observational vector \mathbf{y} , the state vector $\overline{\mathbf{X}}^b$
370 was updated by minimizing the analysis variance.

$$371 \quad \overline{\mathbf{X}}^a = \overline{\mathbf{X}}^b + \mathbf{K}(\mathbf{y} - \mathbf{H}\overline{\mathbf{X}}^b) \quad (8)$$

$$372 \quad \mathbf{K} = \mathbf{P}^b \mathbf{H}^T (\mathbf{H} \mathbf{P}^b \mathbf{H}^T + \mathbf{R})^{-1} \quad (9)$$

$$373 \quad \mathbf{P}^b = \frac{1}{N-1} \sum_{i=1}^N (\mathbf{X}_i^b - \overline{\mathbf{X}}^b \overline{\mathbf{X}}^{bT}) (\mathbf{X}_i^b - \overline{\mathbf{X}}^b \overline{\mathbf{X}}^{bT})^T \quad (10)$$

$$374 \quad \delta\mathbf{X}_i^a = \delta\mathbf{X}_i^b - \tilde{\mathbf{K}} \mathbf{H} \delta\mathbf{X}_i^b \quad (11)$$

375 While employing sequential assimilation and independent observations, $\tilde{\mathbf{K}}$ is
376 calculated as follows:

$$377 \quad \tilde{\mathbf{K}} = \left(1 + \sqrt{\mathbf{R} / (\mathbf{H} \mathbf{P}^b \mathbf{H}^T + \mathbf{R})}\right)^{-1} \mathbf{K} \quad (12)$$

378 where $\overline{\mathbf{X}}^b \overline{\mathbf{X}}^{bT}$ is the mean of the ensemble samples \mathbf{X}_i^b ; \mathbf{H} is the observation operator
379 that maps ~~simulated concentrations from~~ the model space to the observation space.

380 consisting of the model integration process converting emissions into concentrations
381 and spatial interpolation matching the model concentration to the locations of the
382 observations; $\mathbf{y} - \mathbf{H}\bar{\mathbf{X}}^b$ reflects the differences between the simulated and observed
383 concentrations; \mathbf{P}^b is the ensemble-estimated background (a priori) error covariance;
384 $\mathbf{P}^b \mathbf{H}^T$ contains the response of the uncertainty in the simulated concentrations to the
385 uncertainty in emissions; \mathbf{K} is the Kalman gain matrix of the ensemble mean depending
386 on the \mathbf{P}^b and observation error covariance \mathbf{R} , representing the relative contributions
387 to analysis; and $\tilde{\mathbf{K}}$ is the Kalman gain matrix of the ensemble perturbation, which is
388 used to calculate emission perturbations after inversions $\delta \mathbf{X}_i^a$. The ensemble mean $\bar{\mathbf{X}}^a$
389 of the analyzed state was considered the best estimate of the emissions.

390 When large volumes of site observations are at a much higher resolution than the model
391 grid spacing, many correlated or fully consistent model-data mismatch errors can
392 appear in one cluster, resulting in excessive adjustments and deteriorated model
393 performance (Houtekamer and Mitchell, 2001). To reduce the horizontal observation
394 error correlations and influence of representativeness errors, a “super-observation”
395 approach combining multiple noisy observations located within the same grid and
396 assimilation window was developed based on optimal estimation theory (Miyazaki et
397 al., 2012a). Previous studies demonstrated the necessity for data-thinning and
398 dealiasing errors (Feng et al., 2020b; Zhang et al., 2009a). The super-observation y_{new} ,
399 super-observation error r_{new} , and corresponding simulation $x_{new,i}$ of the i th sample
400 are calculated as follows:

$$401 \quad 1/r_{new}^2 = \sum_{j=1}^m 1/r_j^2 \quad (13)$$

$$402 \quad y_{new} = \sum_{j=1}^m w_j y_j / \sum_{j=1}^m w_j \quad (14)$$

$$403 \quad x_{new,i} = \sum_{j=1}^m w_j x_{ij} / \sum_{j=1}^m w_j \quad (15)$$

404 where j is the identifier of m observations within a super-observation grid; r_j is the
405 observational error of the actual j th observation y_j ; x_{ij} is the simulated concentration

406 using the i th prior emission sample corresponding to the j th observation; and $w_j =$
407 $1/r_j^2$ is the weighting factor. The super-observation error decreased as the number of
408 observations used within a super-observation increased. This method was used in our
409 previous inversions using surface-based (Feng et al., 2020b) and satellite-based (Jiang
410 et al., 2021) observations.

411 In this study, the DA window was set to one day because the model requires a longer
412 time to integrate the emission information into the concentration ensembles (Ma et al.,
413 2019). Due to the “super-observation” approach, only one assimilation is needed in one
414 assimilation window. In addition, owing to the complexity of hourly emissions, it is
415 difficult to simulate hourly concentrations that match the observations well. Although
416 a longer DA window would allow more observations to constrain the emission change
417 of one grid, the spurious correlation signals of EnKF would attenuate the observation
418 information over time (Bruhwiler et al., 2005; Jiang et al., 2021). Kang et al. (2012)
419 conducted OSSEs and demonstrated that owing to the transport errors and increased
420 spurious correlation, a longer DA window (e.g. 3 weeks) would cause the analysis
421 system to blur essential emission information away from the observation. Therefore,
422 daily mean simulations and observations were used in the EnSRF algorithm and daily
423 emissions were optimized in this system.

424 EnKF is subject to spurious correlations because of the limited number of ensembles
425 when it is applied in high-dimensional atmospheric models, which can cause rank
426 deficiencies in the estimated background error covariance and filter divergence and
427 further degrade analyses and forecasts (Wang et al., 2020). Covariance localization is
428 performed to reduce spurious correlations caused by a finite ensemble size
429 (Houtekamer and Mitchell, 2001). Covariance localization preserves the meaningful
430 impact of observations on state variables within a certain distance (cutoff radius) but
431 limits the detrimental impact of observations on remote state variables. The localization
432 function of Gaspari and Cohn function (Gaspari and Cohn, 1999) is used in this system,

433 which is a piecewise continuous fifth-order polynomial approximation of a normal
434 distribution. The optimal localization scale is related to the ensemble size, assimilation
435 window, dynamic system, and lifetime of the chemical species in the atmosphere. CO,
436 SO₂ and PM_{2.5} are rather stable in the atmosphere, with a lifetime of more than one day.
437 According to the average wind speed (3.3 m/s, Table 4) and length of the DA window,
438 the localization scales of CO, SO₂ and PM_{2.5} were set to 300 km. In addition, the
439 localization scales of NO₂, which is rather reactive and has a lifetime of approximately
440 10 hours in winter (de Foy et al., 2015), and PMC, which mainly from local sources
441 and has a short residence time in the atmosphere owing to the rapid deposition rate
442 (Clements et al., 2014; Clements et al., 2016; Hinds, 1982), were set to 150 and 250
443 km, respectively.

444 **2.2 Prior emissions and uncertainties**

445 Anthropogenic emissions over China were obtained from the 2016 Multi-resolution
446 Emission Inventory for China (MEIC 2016) (Zheng et al., 2018), while those over the
447 other regions of East Asia were obtained from the mosaic Asian anthropogenic emission
448 inventory (MIX) (Li et al., 2017). The spatial resolutions of the MEIC and MIX
449 inventories were both 0.25° × 0.25° and they are downscaled to match the model grid
450 spacing of 36 km. The spatial distributions of CO, SO₂, NO_x, PPM_{2.5}, and PMC
451 emissions are shown in Figure 112. The daily emission inventory, which was
452 arithmetically averaged from the combined monthly emission inventory, was directly
453 used in the EI subsystem and was employed as the prior emission of the first DA
454 window in the EI subsystem (Figure 1). During the simulations, daily emissions were
455 further converted to hourly emissions. All species emitted from area sources were
456 converted to hourly emissions using the same diurnal profile (Figure S2) and for the
457 point source, we assumed that there was no diurnal change. MEIC 2012 was used as an
458 alternative a priori over China to investigate the impact of different prior emissions on
459 optimized emissions. The Model of Emissions of Gases and Aerosols from Nature
460 (MEGAN) (Guenther et al., 2012) was used to calculate time-dependent biogenic
461 emissions, which was driven by the WRF model. Biomass burning emissions were not

462 included because they have little impact across China during the study period (Zhang
463 et al., 2020).

464 During the inversion cycles, inverted emissions of different members converge
465 gradually, and the ensemble-estimated error covariance matrix is likely to be
466 underestimated. To avoid this, considering the compensation of model errors and
467 comparable emission uncertainties from one day to the next, we imposed the same
468 uncertainty on emissions at each DA window. As mentioned above, the optimized
469 emissions of the current DA window were transferred to the next DA window as prior
470 emissions. The technology-based emission inventory developed by Zhang et al. (2009b),
471 using the same method as MEIC, showed that the emissions of PMC and PPM_{2.5} had
472 the largest uncertainties, followed by CO, and finally SO₂ and NO_x. Therefore, the
473 uncertainties of PMC, PPM_{2.5}, CO, SO₂, and NO_x in this study were set as 40%, 40%,
474 30%, 25%, and 25%, respectively. However, previous studies have shown that inversely
475 estimated CO and PMC emissions can exceed 100% higher than the bottom-up
476 emissions (MEIC) in certain areas (Feng et al., 2020b; Ma et al., 2019). Therefore,
477 according to the extent of underestimation, we set an uncertainty of 100% for both the
478 CO and PMC emissions at the beginning of the three DA windows to quickly converge
479 the emissions. Mean emission analysis is generally minimally sensitive to the
480 uncertainty setting in the assimilation cycle method (Feng et al., 2020; Gurney et al.,
481 2004; Miyazaki et al., 2012a) as the inversion errors of the current window can be
482 transferred to the next window for further optimization (Section 4.3).

483 **2.3 Observation data and errors**

484 Hourly averaged surface CO, SO₂, NO₂, O₃, PM_{2.5}, and PM₁₀ observations from 1504
485 national control air quality stations were assimilated into this system, which were
486 obtained from the Ministry of Ecology and Environment of the People's Republic of
487 China (<http://106.37.208.233:20035/>, last access: 25 June 2020). These sites are
488 distributed over most of central and eastern China and become denser near metropolitan
489 areas (see Figure 2). To ensure data quality, value-range checks were performed to
490 eliminate unrealistic or unrepresentative observations and only the observations within

491 the subjectively selected threshold range were assimilated (Table 2). In additionally, a
 492 time-continuity check was performed to eliminate gross outliers and sudden anomalies
 493 using the function of $\max(|O(t) - O(t \pm 1)|) \leq f(t)$, where $O(t)$ and $O(t \pm 1)$
 494 represent observations at time t and $t \pm 1$, respectively, and $f(t) = T_a + T_b \times O_t$.
 495 This means that the concentration difference between time t and time $t+1$ and $t-1$ should
 496 be less than $f(t)$. T_b was fixed at 0.15 and the section of T_a is given in Table 2,
 497 which was determined empirically according to the time series change of concentration
 498 at each site. To avoid potential cross-correlations, we assimilated PM_{2.5} and PMC.
 499 Additionally, in the EI subsystem, the observations within each city were averaged to
 500 reduce the data density, reduce the error correlation, and increase spatial representation
 501 (Houtekamer and Mitchell, 2001; Houtekamer and Zhang, 2016). Finally, 336 city sites
 502 were available across mainland China, in which data from 311 cities were selected for
 503 assimilation and the remaining 25 were selected for independent validation (Figure 2).
 504 In the IA subsystem, owing to the small horizontal correlation scale (Figure 3), all site
 505 observations were assimilated to provide a good IC for the next emission inversion to
 506 obtain more extensive observation constraints.

507 The observation error covariance matrix (\mathbf{R}) includes both the measurement and
 508 representation errors. The measurement error ε_0 is defined as follows:

$$509 \quad \varepsilon_0 = ermax + ermin \times \Pi_0 \quad (16)$$

510 where $ermax$ is the base error and Π_0 denotes the observed concentration. These
 511 parameters for different species are listed in Table 2 and were determined according to
 512 Chen et al. (2019), Feng et al. (2018), and Jiang et al. (2013b).

513 The representative error depends on the model resolution and characteristics of the
 514 observation locations, which were calculated using the equations of Elbern et al. (2007),
 515 defined as follows:

$$516 \quad \varepsilon_r = \gamma \varepsilon_0 \sqrt{\Delta l / L} \quad (17)$$

517 where γ is a tunable parameter (here, $\gamma=0.5$), Δl is the grid spacing (36 km), and L

518 is the radius (3 km for simplification) of the influence area of the observation. The total
 519 observation error (r) was defined as follows:

$$520 \quad r = \sqrt{\varepsilon_0^2 + \varepsilon_r^2} \quad (18)$$

521 **Table 2.** Parameters of quality control and measurement error

| Parameter | CO mg m ⁻³ | SO ₂ μg m ⁻³ | NO ₂ μg m ⁻³ | O ₃ μg m ⁻³ | PM _{2.5} μg m ⁻³ | PMC μg m ⁻³ |
|------------------------------|--------------------------|---------------------------------------|---------------------------------------|--------------------------------------|---|---------------------------|
| value-range | 0.1-12 | 1-800 | 1-250 | 1-250 | 1-800 | 1-900 |
| time-continuity (T_a) | 2.5 | 160 | 70 | 80 | 180 | 180 |
| ermax | 0.05 | 1 | 1 | 1 | 1.5 | 1.5 |
| ermin | 0.5% | 0.5% | 0.5% | 0.5% | 0.75% | 0.75% |

522

523 **3 Experimental design**

524 RAPAS was conducted according to the procedure and settings described in Section 2.
 525 December is one of the months with the most severe air pollution, whereas July is one
 526 of the least polluted months in China. Therefore, this study mainly tested the
 527 performance of the RAPAS system over these two months. For December, the IA
 528 subsystem was run from 26 November to 31, 2016, with a 6-hour interval cycling
 529 assimilation to optimize ICs (ICDA). A better IC at 0000 UTC on 1 December could be
 530 obtained by a five-day high-frequency cycling assimilation and atmospheric mixing.
 531 The EI subsystem was then run for December 2016 with a one-day assimilation window
 532 to optimize emissions (EMDA). In July, the system operated identically to that of
 533 December. It should be noted that owing to the stronger atmospheric oxidation, the
 534 lifetime of NO₂ in July was significantly shorter than that in December; thus, we
 535 adopted a smaller localization scale for NO₂ (80 km). Both assimilation experiments
 536 used the combined prior emission inventories of 2016, as described in Section 2.2, and
 537 the emission base year coincided with the research stage. An Observing Systems
 538 Simulation Experiment (OSSE) was conducted to evaluate the performance of the

539 RAPAS system, which has been widely used in previous assimilation systems
540 development (Daley, 1997). In the OSSE experiment, we used the MEIC 2016
541 inventory as a “true” emission and reduced by 30% over mainland China as a prior
542 emission. The simulations were simulated using the “true” emission and sampled
543 according to the locations and times of the real observations used as artificial
544 observations. The observation errors were the same as those in EMDA. To evaluate the
545 IC improvements from the IA subsystem, an experiment without 3DVAR (NODA) was
546 conducted with the same meteorological fields and physical and chemistry
547 parameterization settings as those of the ICDA. To evaluate the posterior emissions of
548 the EI subsystem, two parallel forward modelling experiments were performed for
549 December 2016: a control experiment (CEP) with prior (MEIC 2016) emissions and a
550 validation experiment (VEP) with posterior emissions. Both experiments used the same
551 IC at 0000 UTC on December 01 generated through the IA subsystem. The only
552 difference between CEP and VEP were emissions. Table 3 summarizes the different
553 emission inversion experiments conducted in this study.

554 To investigate the robustness of our system, eight sensitivity tests (from EMS1 to
555 EMS78; see Table 3) were performed. These experiments were all based on EMDA. ~~In~~
556 ~~EMS1, rather than forward simulation using the optimized emissions of the previous~~
557 ~~DA window in EMDA, the ICs of each DA window were first taken from the forward~~
558 ~~simulation with the prior emissions of the previous DA window and then optimized~~
559 ~~using the EnSRF algorithm and the observations at the corresponding moment, as~~
560 ~~mentioned in Section 2.3. The objective of this experiment was to investigate the~~
561 ~~advantages of the “two-step” calculation scheme in the EI subsystem.~~ EMS12 used
562 MEIC 2012 as the original prior emission in China, aiming to investigate the impact of
563 different prior inventories on the estimates of emissions. The other experiments
564 (EMS23–56) aimed to test the impact of different prior uncertainty settings, in which
565 the prior uncertainties were reduced by -50% and -25%, and increased by 25% and 50%,
566 respectively. EMS67 aimed to evaluate the impact of observation errors on emission
567 estimates, in which all observation errors are magnified twice. EMS78 aimed to

568 evaluate the impact of IC optimization of the first window on emission estimates, in
 569 which the ICs were taken from a five-day spin-up simulation. Eight forward modelling
 570 experiments (VEP1, VEP2, ..., VEP78) were also performed with the posterior
 571 emissions of EMS1 to EMS78 to evaluate their performance.

572 **Table 3.** Emission inversion and sensitivity experiments conducted in this study

| Exp. Type | Exp. Name | Period | IC of the first DA Window | ICs of the subsequent DA window | Emission |
|--------------|-------------------------|--------------------------|---|--|--|
| Assimilation | EMDA | 1–31 December | 0000 UTC on December 1, taken from ICDA | Forecast with posterior emissions in the previous window | MEIC 2016 for December (the first DA window), optimized emissions of the previous window (other DA windows) |
| | OSSE | 1–31 December | Same as EMDA | Same as EMDA | Same as EMDA but with a decrease of 30% for CO, SO ₂ , NO _x , PPM _{2.5} , and PMC |
| Sensitivity | EMS1 | 1–31 December | Same as EMDA | Optimized using the EnSRF DA method | Same as EMDA |
| | EMS12 | 1–31 December | Same as EMDA | Same as EMDA | Same as EMDA but for EMIC 2012 |
| Sensitivity | EMS3-62-5 | 1–31 December | Same as EMDA | Same as EMDA | Same as EMDA but with a ± 25% or ± 50% of default uncertainty |
| | EMS7E MS6 | 1–31 December | Same as EMDA | Same as EMDA | Same as EMDA but with a +100% of default observation errors |
| | EMS8E MS7 | 1–31 December | 0000 UTC on December 1, taken from ICNO | Same as EMDA | Same as EMDA |

573

574 **4 Results**

575 **4.1 Evaluations**

576 **4.1.1 Simulated meteorological fields**

577 In the RAPAS system, the inversion approach attributes all biases between the
578 simulated and observed concentrations to emissions. Meteorological fields dominate
579 the physical and chemical processes of air pollutants in the atmosphere, and thus their
580 simulation accuracy would significantly affect the estimates of emissions in this study.
581 To quantitatively evaluate the performance of the WRF simulations, the mean bias
582 (BIAS), root mean square error (RMSE), and correlation coefficient (CORR) were
583 calculated against the surface meteorological observations measured at 400 stations and
584 the planetary boundary layer height (PBLH) was calculated using the sounding data at
585 92 sites. Surface observations were obtained from the National Climate Data Center
586 integrated surface database (<http://www.ncdc.noaa.gov/oa/ncdc.html>, last access: 25
587 October 2021) and sounding data were obtained from the website of the University of
588 Wyoming (<http://weather.uwyo.edu/upperair/sounding.html>, last access: 10 March
589 2022). The sounding data had a 12 hour interval. The observed PBLH was calculated
590 using sound data via the bulk Richardson number method (Richardson et al., 2013).
591 The spatial distribution of meteorological stations is shown in Figure 2. The simulated
592 temperature at 2 m (T2), relative humidity at 2 m (RH2), wind speed at 10 m (WS10),
593 and PBLH from 26 November to 31 December 2016 were evaluated against the
594 observations. Table 4 summarizes the statistical results of the evaluation of the
595 simulated meteorological parameters. Overall, T2, RH2 and PBLH were slightly
596 underestimated, with biases of -0.1 °C, -3.8%, and -41.1 m, respectively. CORRs were
597 approximately 0.98 for T2, 0.94 for RH2, and 0.90 for PBLH, showing good
598 consistency between the observations and simulations. WS10 was overestimated, with
599 a bias of 0.7 m/s and an RMSE of 0.8 m/s, but were better than the simulations from
600 many previous studies (Chen et al., 2016; Jiang et al., 2012a; Jiang et al., 2012b).
601 Therefore, the WRF can generally reproduce meteorological conditions sufficiently in

602 terms of their temporal variation and magnitude over China, which is adequate for our
 603 inversion estimation.

604 **Table 4.** Statistics comparing the simulated and observed 10-m wind speed (WS10), 2-
 605 m temperature (T2), and 2-m relative humidity (RH2), and planetary boundary layer
 606 height (PBLH).

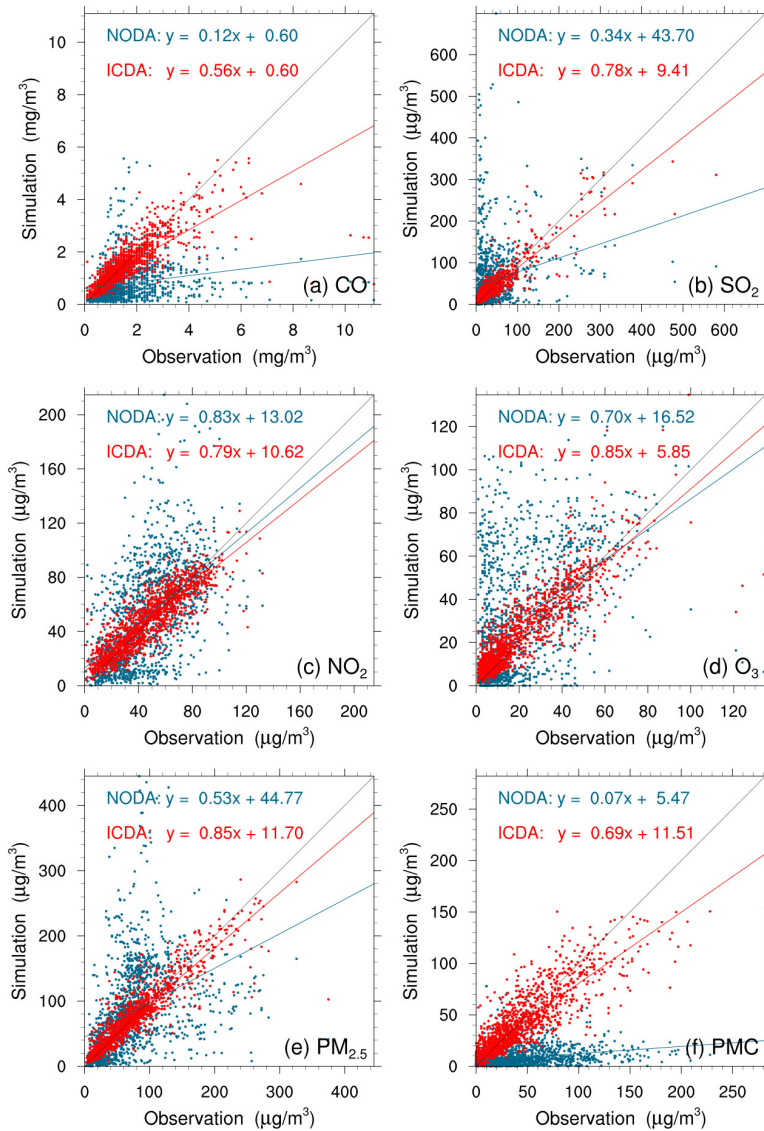
| Variable Met. | No. of sites | Mean Obs. | Mean Sim. | BIAS | RMSE | CORR |
|---------------|--------------|-----------|-----------|-------|------|------|
| WS10 (m/s) | 400 | 2.6 | 3.3 | 0.7 | 0.8 | 0.72 |
| T2 (°C) | 400 | 2.9 | 2.8 | -0.1 | 0.7 | 0.98 |
| RH2 (%) | 400 | 66.3 | 62.6 | -3.8 | 5.2 | 0.94 |
| PBLH (m) | 92 | 267.5 | 226.4 | -41.1 | 50.4 | 0.90 |

607 * BIAS, mean bias; RMSE, root mean square error; CORR, correlation coefficient

608 4.1.2 Initial conditions

609 Figure 4 shows an evaluation of the analyzed concentrations of the six species against
 610 surface observations. For comparison, the evaluations of the simulations without
 611 3DVAR (NODA) are also shown in Figure 4. The simulations of the NODA experiment
 612 (red dots) are scattered on both sides of the central line, as large systematic biases
 613 remain across many measurement sites. Conversely, the ICDA experiment (blue dots)
 614 showed a much better agreement with the observations than those from NODA. The
 615 statistics show that there are large systematic biases in the NODA simulations, with
 616 large RMSEs and small CORRs for all species, particularly for CO and PMC. After the
 617 assimilation of surface observations, the RMSE of CO decreased to 0.7 mg m⁻³, and
 618 those of SO₂, NO₂, O₃, PM_{2.5}, and PMC decrease to 22.0, 12.0, 9.6, 20.5, and 19.6 μg
 619 m⁻³, respectively, with respective reductions of 50.0%, 73.1%, 61.0%, 64.7%, 69.5%,
 620 and 60.8% compared to those of the NODA (Table 5). The CORRs of ICDA increased
 621 by 290.0%, 291.3%, 55.4%, 87.2%, 130.0%, and 214.8% to 0.78, 0.90, 0.87, 0.88, 0.92,
 622 and 0.85, respectively. These statistics indicate that the ICs of the ground level
 623 improved significantly. However, owing to the lack of observations, we still do not

624 know the simulation bias in the upper-middle boundary layer. Although concentrations
625 at high altitudes can be constrained by ground-based observations through vertical
626 correlations, the effect is limited; therefore, the bias remains non-negligible.



627

628 **Figure 4.** Scatter plots of simulated versus observed (a) CO, (b) SO₂, (c) NO₂, (d) O₃,
629 (e) PM_{2.5}, and (f) PMC mass concentrations at 0000 UTC on December 1 initializations
630 from the background (red) and analysis (blue) fields.

631

632

633

634 **Table 5.** Comparisons of the surface CO, SO₂, NO₂, O₃, PM_{2.5}, and PMC mass
 635 concentrations from the control and assimilation experiment against observations
 636 aggregated over all analysis times. CO unit: mg m⁻³; others units: µg m⁻³.

| Species | Exp. Name | Mean Obs. | Mean Sim. | BIAS | RMSE | CORR |
|-------------------|-----------|-----------|-----------|-------|------|------|
| CO | NODA | 1.5 | 0.8 | -0.7 | 1.4 | 0.20 |
| | ICDA | | 1.5 | -0.1 | 0.7 | 0.78 |
| SO ₂ | NODA | 36.3 | 56.0 | 19.7 | 81.7 | 0.23 |
| | ICDA | | 37.8 | 1.5 | 22.0 | 0.90 |
| NO ₂ | NODA | 45.8 | 51.1 | 5.3 | 30.8 | 0.56 |
| | ICDA | | 47.0 | 1.1 | 12.0 | 0.87 |
| O ₃ | NODA | 20.5 | 30.8 | 10.4 | 27.2 | 0.47 |
| | ICDA | | 23.3 | 2.8 | 9.6 | 0.88 |
| PM _{2.5} | NODA | 70.9 | 82.2 | 11.3 | 67.3 | 0.40 |
| | ICDA | | 71.8 | 0.9 | 20.5 | 0.92 |
| PMC | NODA | 43.5 | 8.5 | -35.0 | 50.0 | 0.27 |
| | ICDA | | 41.6 | -1.9 | 19.6 | 0.85 |

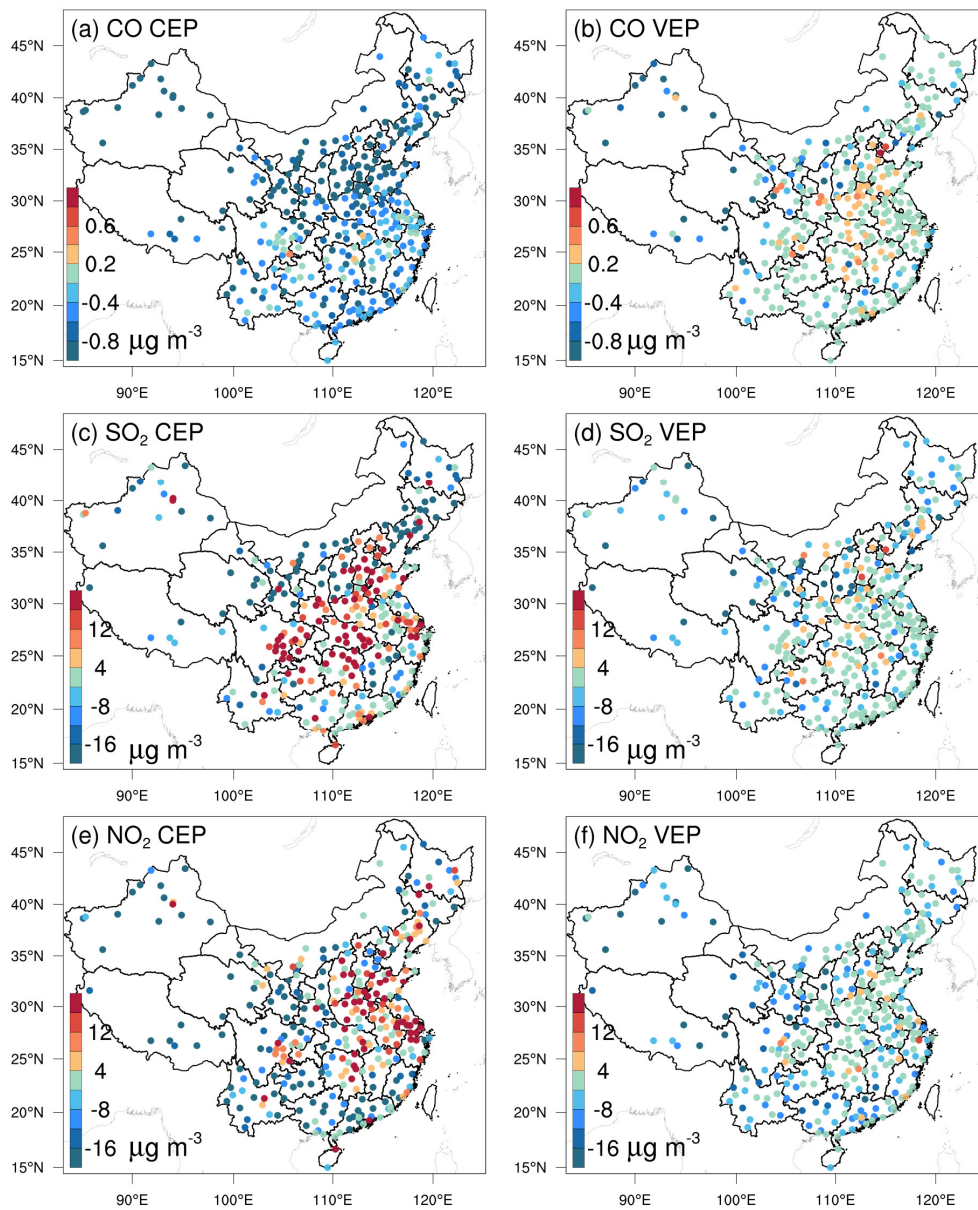
637 * BIAS, mean bias; RMSE, root mean square error; CORR, correlation coefficient

638 4.1.3 Posterior emissions

639 Owing to the mismatched spatial scales, it is difficult to directly evaluate the optimized
 640 emissions against observations. Generally, we indirectly validated the optimized
 641 emissions by comparing the forward simulated concentrations using the posterior
 642 emissions against atmospheric measurements (e.g., Jiang et al., 2014; Jin et al., 2018;
 643 Peters et al., 2007). Figure 5 shows the spatial distributions of the mean biases between
 644 the gaseous pollutants simulated using prior and posterior emissions and assimilated
 645 observations. In the CEPs, for each species, the distribution of biases was similar to the
 646 increments in background fields constrained through 3DVAR, as shown in Figure S3.
 647 For example, almost all sites had large negative biases for CO, while for SO₂ and NO₂,
 648 positive biases were mainly distributed over the North China Plain (NCP), Yangtze
 649 River Delta (YRD), Sichuan Basin (SCB), and Central China and negative biases were
 650 distributed over remaining areas. After constraining with observations, the biases of all

651 three gaseous air pollutants were significantly reduced at most sites. For CO, the biases
652 at 62% of the sites decreased to absolute values less than 0.2 mg m^{-3} and for SO₂ and
653 NO₂, the biases at 52% and 47% of the sites were within $\pm 4 \text{ } \mu\text{g m}^{-3}$. However, large
654 negative biases were still observed in western China, indicating that the uncertainties
655 of the posterior emissions are still large in western China, which may be attributed to
656 the large biases in prior emissions and the relatively limited observations. Overall, the
657 statistics show that there are different levels of improvement at the 311 assimilation
658 sites of 92%, 85%, and 85% for CO, SO₂, and NO₂, respectively. The small number of
659 sites with worse performance may be related to over-adjusted emissions by EI or
660 contradictory adjustments caused by opposite biases in adjacent areas.

661 Table 6 lists the statistical results of the evaluations averaged over the whole mainland
662 of China. For CO, the mean bias was -0.8 mg m^{-3} with the prior emissions, while it
663 substantially reduced to -0.1 mg m^{-3} (reduction rate of 89.6%) when simulating with
664 the posterior emissions. Additionally, the RMSE decreased by 48.1% from 1.08 to 0.56
665 mg m^{-3} , and the CORR increased by 76.1% from 0.46 to 0.81. For SO₂ and NO₂, the
666 regional mean biases slightly increased as the positive/negative biases among different
667 sites might be offset. However, the RMSEs decreased to 17.7 and 12.3 $\mu\text{g m}^{-3}$,
668 respectively, which were 58.3% and 50.8% lower than those of CEPs, and the CORRs
669 increased by 125.6% and 35.4%, both reaching up to 0.88, indicating that EI
670 significantly improved the NO_x and SO₂ emission estimates.

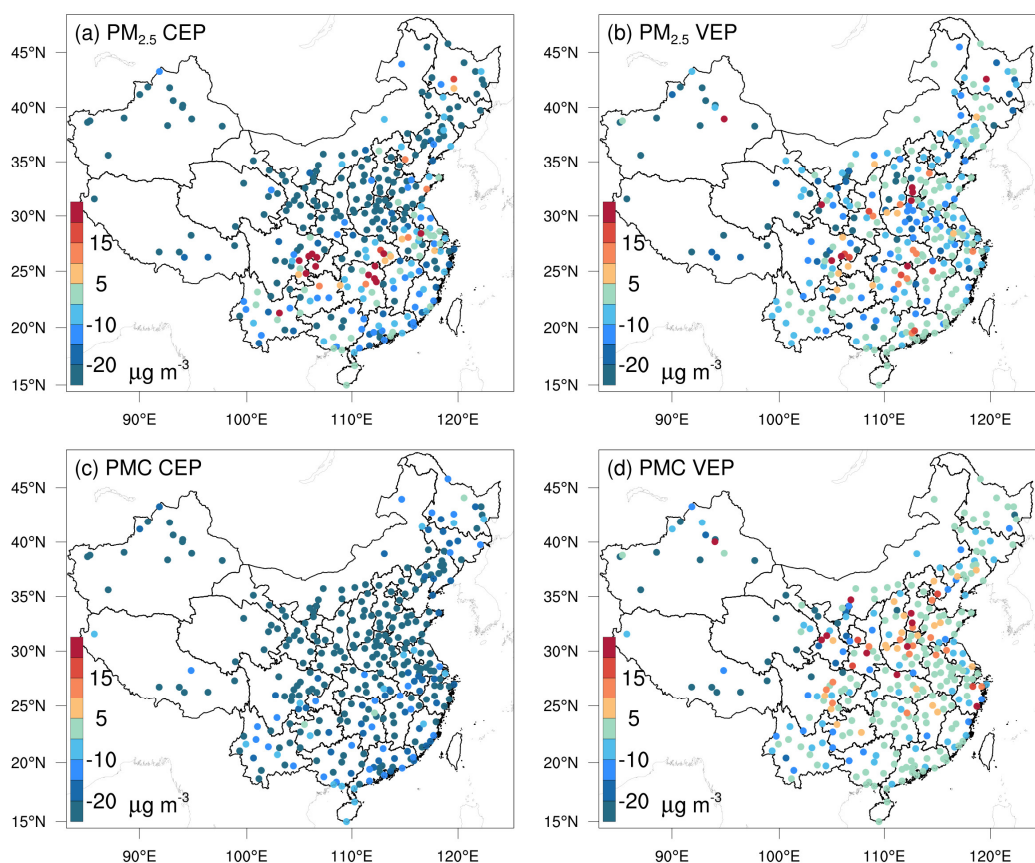


671

672 **Figure 5.** Spatial distribution of the BIAS of the simulated (a, b) CO, (c, d) SO₂, and
 673 (e, f) NO₂ with prior (left, CEP) and posterior (right, VEP) emissions. CO unit: mg m⁻³
 674 ³; SO₂ and NO₂ units: µg m⁻³.

675 Figure 6 shows the spatial distributions of the mean biases of simulated PM_{2.5} and PMC
 676 evaluated against assimilated observations. Similarly, the CEP simulations did not
 677 perform well. There were widespread underestimations across the country, with mean
 678 biases of -24.0 and -32.4 µg m⁻³. After data assimilation, the performance of the VEP
 679 simulations significantly improved. The biases decreased by 72.1% and 90.4% to -6.7

680 and $-3.1 \mu\text{g m}^{-3}$, the RMSEs decreased by 41.2% and 40.7% to 29.6 and $24.6 \mu\text{g m}^{-3}$,
 681 and the CORRs increased by 35.9% and 176.0% to 0.87 and 0.69 for $\text{PM}_{2.5}$ and PMC,
 682 respectively. Overall, 89.6% and 97.2% of the assimilation sites were improved for
 683 $\text{PM}_{2.5}$ and PMC, respectively. However, compared with the results for the three gaseous
 684 pollutants, there were sites with large biases scattered throughout the entire domain. In
 685 addition to the potential over-adjusted or contradictory adjustments of emissions as in
 686 the three gas species, the sites with large biases may be related to the complex
 687 precursors and complex homogeneous and heterogeneous chemical reactions and
 688 transformation processes of secondary $\text{PM}_{2.5}$, and the fact that we did not simulate the
 689 time variation of dust blowing caused by wind speed for PMC owing to the lack of land
 690 cover data that is compatible with the CMAQ dust module and agricultural activity data
 691 to identify dust source regions.

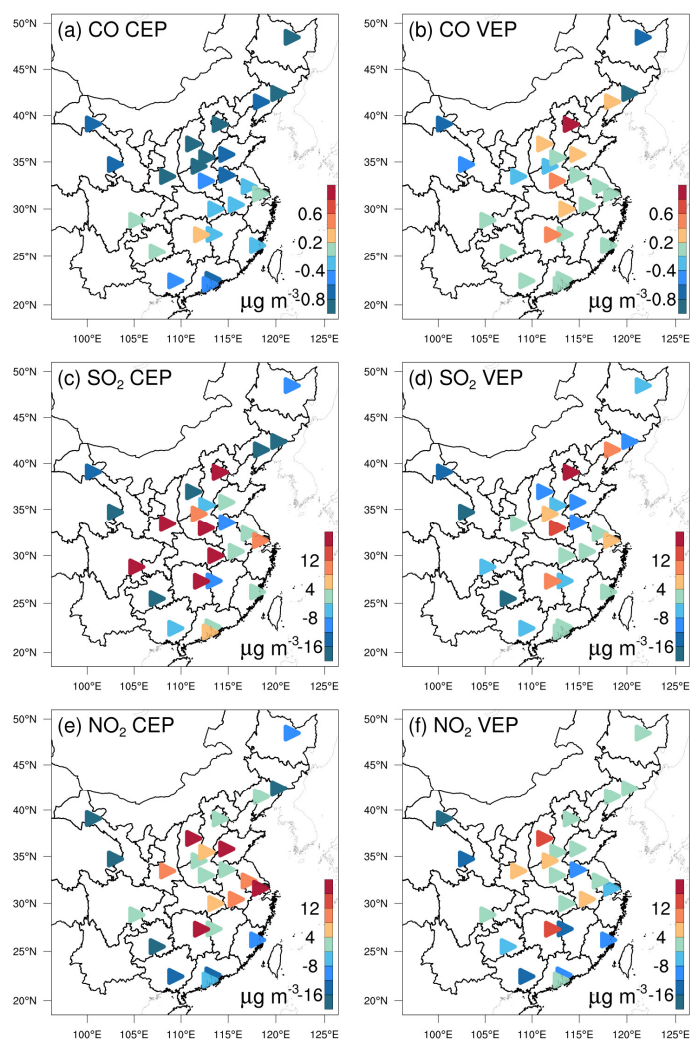


692

693

Figure 6. Same as in Figure 5 but for $\text{PM}_{2.5}$ and PMC.

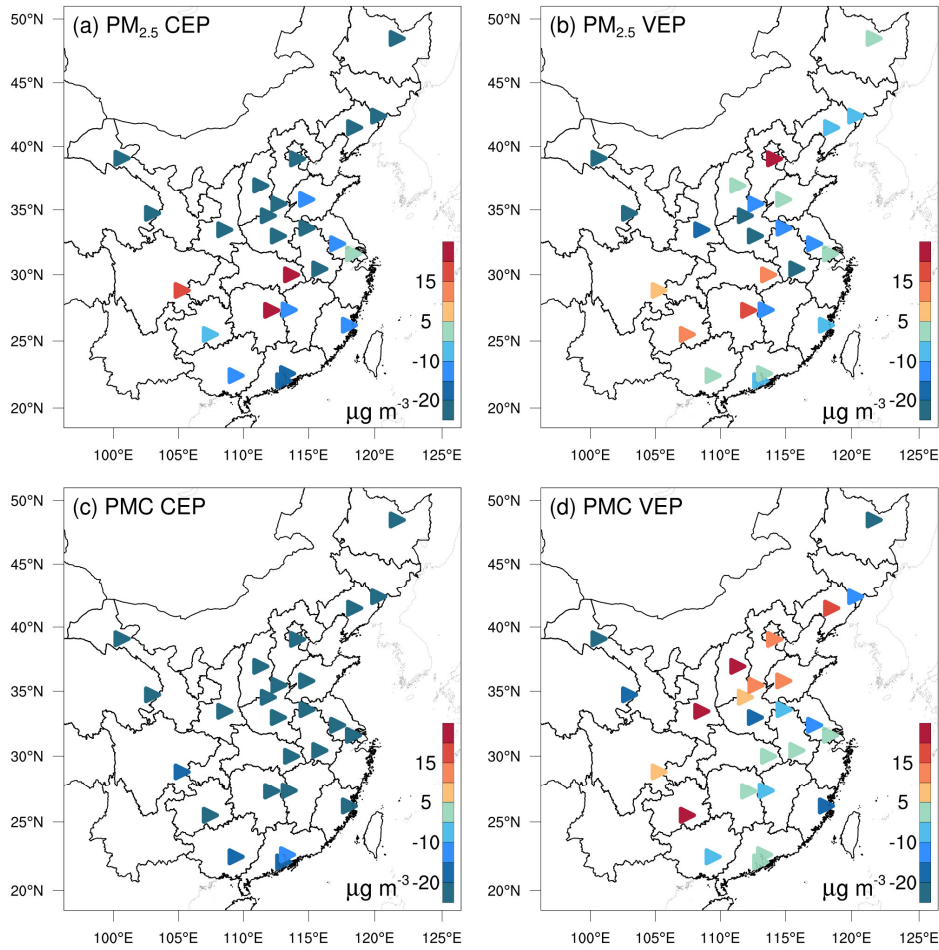
694 Figures 7 and 8 show the spatial distributions of the biases calculated against
 695 independent observations for the five species. With posterior emissions, the decreasing
 696 ratios of RMSEs ranged from 26.7%–42.0% and the CORRs increased by 13.7–59.0%
 697 to 0.62–0.87. Overall, the biases at the independent sites are similar or slightly worse
 698 than those at the assimilated sites, which is reasonable as the closer the independent
 699 sites are to the assimilated site, the more constraints of observation information can be
 700 obtained and the more significant the improvements in the optimized state variables of
 701 the model. For example, generally, the transmission distance of NO₂ is relatively short
 702 and remote cities with small emission correlations to the cities with assimilated
 703 observations are relatively less constrained, resulting in only a 26.7% decrease in the
 704 RMSE.



705

706

Figure 7. As in Figure 5 but for the independent validation.



707
708

Figure 8. As in Figure 6 but for the independent validation.

709 Comparing our results with those of previous studies, Tang et al. (2013) inverted CO
 710 emissions over Beijing and the surrounding areas and obtained comparable
 711 improvements (Table 6) in the RMSE (37–48% vs. 30–51%) and CORR (both studies
 712 ~ 0.81); however, we decreased the biases by 90–97%, which is much greater than their
 713 48–64% reductions. Additionally, Chen et al. (2019) showed that the RMSE of
 714 simulated SO₂ with updated SO₂ emissions decreased by 4.2–52.2% for different
 715 regions, and the CORR only increased to 0.69 at most. These improvements are smaller
 716 than those obtained in this study, which may be due to the insufficient adjustment of
 717 emissions caused by the underestimated ensemble spread through the inflation method.
 718 The better performance in this study may be related to our inversion process, which
 719 causes the optimized emissions of the current DA window to propagate to the next DA
 720 window for further correction.

721 **Table 6.** Statistics comparing the pollution concentrations from the simulations with
 722 prior (CEP) and posterior (VEP) emissions against assimilated and independent
 723 observations, respectively. CO unit: mg m⁻³; others units: µg m⁻³.

| Species | Mean Obs. | Mean Sim. | | BIAS | | RMSE | | CORR | |
|----------------------------------|-----------|-----------|------|-------|-------|------|------|------|------|
| | | CEP | VEP | CEP | VEP | CEP | VEP | CEP | VEP |
| Against assimilated observations | | | | | | | | | |
| CO | 1.43 | 0.66 | 1.36 | -0.77 | -0.08 | 1.08 | 0.56 | 0.46 | 0.81 |
| SO ₂ | 32.5 | 34.4 | 28.4 | 1.9 | -4.1 | 42.4 | 17.7 | 0.39 | 0.88 |
| NO ₂ | 43.8 | 40.8 | 39.0 | -2.9 | -4.8 | 25.0 | 12.3 | 0.65 | 0.88 |
| PM _{2.5} | 77.0 | 53.1 | 70.3 | -24.0 | -6.7 | 50.3 | 29.6 | 0.64 | 0.87 |
| PMC | 40.5 | 8.1 | 37.5 | -32.4 | -3.1 | 41.5 | 24.6 | 0.25 | 0.69 |
| Against independent observations | | | | | | | | | |
| CO | 1.54 | 0.79 | 1.52 | -0.75 | -0.02 | 1.15 | 0.72 | 0.59 | 0.82 |
| SO ₂ | 40.6 | 39.2 | 37.3 | -1.3 | -3.2 | 44.3 | 27.2 | 0.57 | 0.87 |
| NO ₂ | 50.2 | 50.0 | 47.5 | -0.3 | -2.7 | 21.7 | 15.9 | 0.73 | 0.83 |
| PM _{2.5} | 91.5 | 64.6 | 84.1 | -26.9 | -7.4 | 64.1 | 37.2 | 0.62 | 0.87 |
| PMC | 42.0 | 9.2 | 40.4 | -32.8 | -1.6 | 39.3 | 26.6 | 0.39 | 0.62 |

724 * BIAS, mean bias; RMSE, root mean square error; CORR, correlation coefficient

725 4.1.4 Uncertainty reduction

726 The uncertainty reduction rate (UR) is an important quantity to evaluate the
 727 performance of RAPAS and the effectiveness of *in situ* observations (Chevallier et al.,
 728 2007; Jiang et al., 2021; Takagi et al., 2011). Following Jiang et al. (2021), the UR was
 729 calculated as

$$730 \quad UR = \left(1 - \frac{\sigma_{posterior}}{\sigma_{prior}}\right) \times 100 \quad (19)$$

731 where $\sigma_{posterior}$ and σ_{prior} are the posterior and prior uncertainties, respectively,
 732 calculated using the standard deviations of the prior and posterior perturbations (Text
 733 S2). [Figure 9](#) [Table 7](#) shows the URs averaged in each province and mainland China.
 734 URs varied with species as they are closely related to the magnitude settings of prior
 735 uncertainties (Jiang et al., 2021). The URs of PPM_{2.5} and PMC were the most effective
 736 while the UR of NO_x emissions was the lowest. For mainland China overall,
 737 uncertainties were reduced by 44.4%, 45.0%, 34.3%, 51.8%, and 56.1% for CO, SO₂,

738 NO_x, PPM_{2.5}, and PMC, respectively. For one species, URs varied across provinces.
 739 URs are usually related to observation coverage, which means that the more observation
 740 constraints there are, the more URs decrease. Additionally, URs may also be related to
 741 emission distributions. Generally, URs were more significant in the provinces where
 742 observations and emissions were both relatively concentrated (e.g. Tibet), while they
 743 were much lower where the emissions were scattered or relatively uniform, but the
 744 observations were only in large cities, even if there were many more observations than
 745 in other provinces.

746 **Table 7. Time-averaged posterior emission uncertainty reduction (%) indicated by the**
 747 **standard deviation reduction of total emissions per province calculated by prior and**
 748 **posterior ensembles.**

| Province | CO | SO ₂ | NO _x | PPM _{2.5} | PMC |
|--------------|------|-----------------|-----------------|--------------------|------|
| Mainland | 44.4 | 45.0 | 34.3 | 51.8 | 56.1 |
| Shanghai | 16.9 | 16.7 | 20.8 | 24.7 | 18.5 |
| Jiangsu | 17.7 | 25.3 | 29.3 | 34.1 | 52.3 |
| Zhejiang | 24.7 | 13.3 | 17.9 | 42.4 | 31.4 |
| Anhui | 20.1 | 52.7 | 39.1 | 58.1 | 40.9 |
| Shandong | 32.1 | 30.0 | 20.3 | 53.7 | 26.7 |
| Beijing | 28.2 | 6.2 | 37.0 | 43.3 | 31.4 |
| Tianjin | 20.0 | 7.0 | 21.4 | 41.3 | 17.8 |
| Hebei | 29.5 | 40.2 | 28.8 | 56.0 | 30.3 |
| Shanxi | 38.4 | 37.9 | 22.5 | 55.3 | 35.0 |
| Neimenggu | 30.1 | 45.8 | 40.4 | 37.6 | 52.8 |
| Henan | 27.4 | 16.1 | 21.9 | 53.7 | 30.8 |
| Hunan | 36.0 | 27.7 | 34.4 | 16.9 | 41.6 |
| Hubei | 30.8 | 16.6 | 26.0 | 46.4 | 46.5 |
| Jiangxi | 20.9 | 28.4 | 29.4 | 47.0 | 46.7 |
| Guangdong | 31.2 | 14.9 | 41.1 | 53.1 | 46.4 |
| Guangxi | 22.6 | 13.9 | 42.5 | 48.1 | 55.2 |
| Fujian | 9.9 | 8.1 | 31.9 | 31.6 | 49.2 |
| Hainan | 0.6 | 0.5 | 4.5 | 0.7 | 23.3 |
| Liaoning | 35.6 | 34.6 | 19.0 | 33.9 | 54.0 |
| Heilongjiang | 29.9 | 27.7 | 17.4 | 42.0 | 65.2 |
| Jilin | 27.9 | 44.5 | 18.7 | 42.0 | 42.8 |
| Shaanxi | 41.3 | 13.2 | 29.8 | 47.9 | 43.1 |
| Gansu | 24.8 | 36.1 | 33.7 | 46.3 | 56.4 |
| Xinjiang | 38.3 | 27.9 | 20.2 | 46.3 | 66.5 |
| Qinghai | 53.9 | 25.8 | 27.3 | 46.0 | 57.9 |
| Ningxia | 47.0 | 36.6 | 17.6 | 38.0 | 30.1 |
| Sichuan | 29.4 | 25.0 | 39.5 | 61.1 | 46.5 |
| Chongqing | 5.7 | 8.2 | 8.8 | 12.7 | 13.8 |
| Guizhou | 14.4 | 16.4 | 26.6 | 40.3 | 38.2 |
| Yunnan | 38.3 | 29.9 | 31.4 | 40.1 | 55.9 |
| Tibet | 30.2 | 0.5 | 52.8 | 67.3 | 73.2 |

749

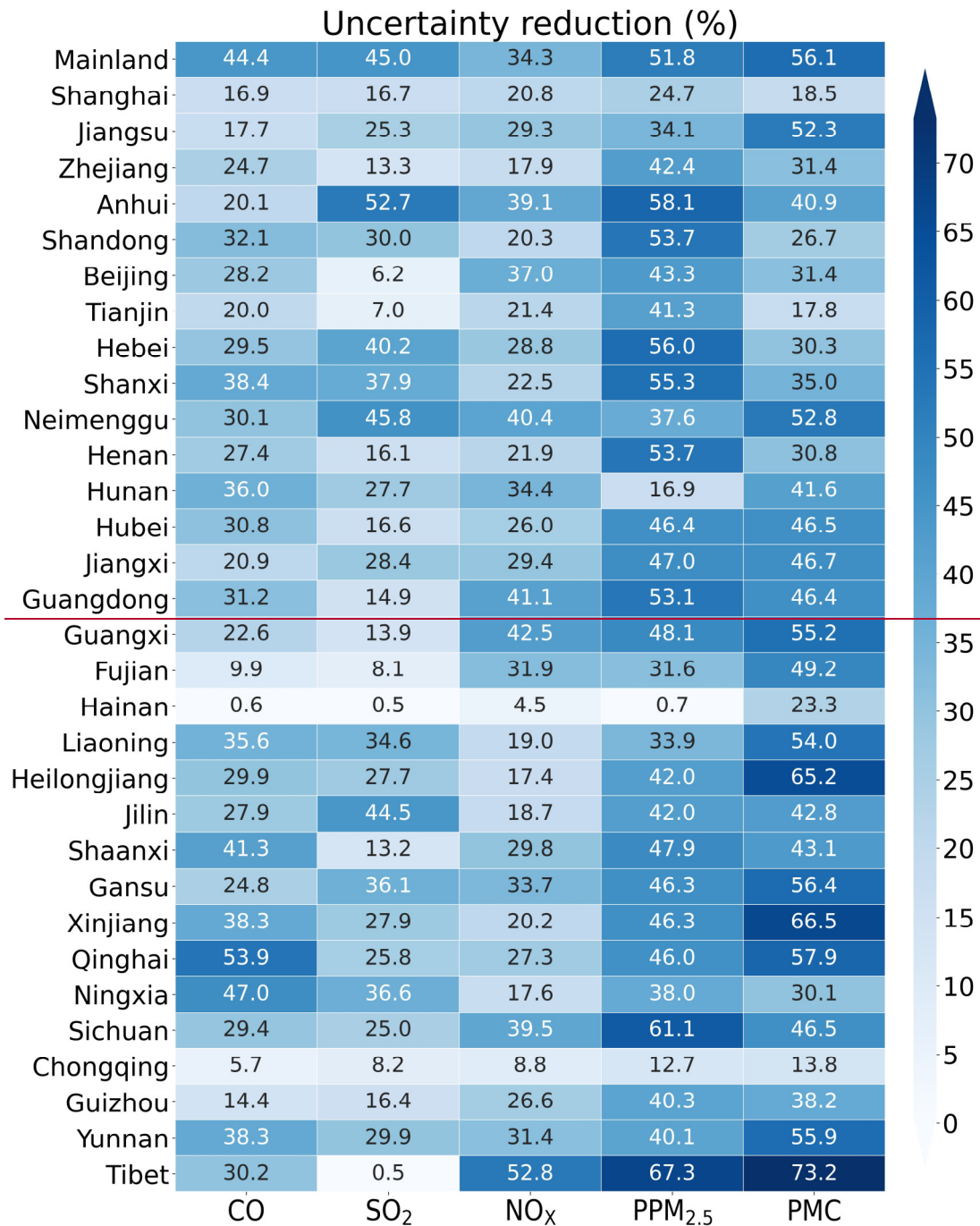


Figure 9. Time-averaged posterior emission uncertainty reduction (%) indicated by the standard deviation reduction of total emissions per province calculated by prior and posterior ensembles.

4.1.5 Evaluation using chi-squared statistics

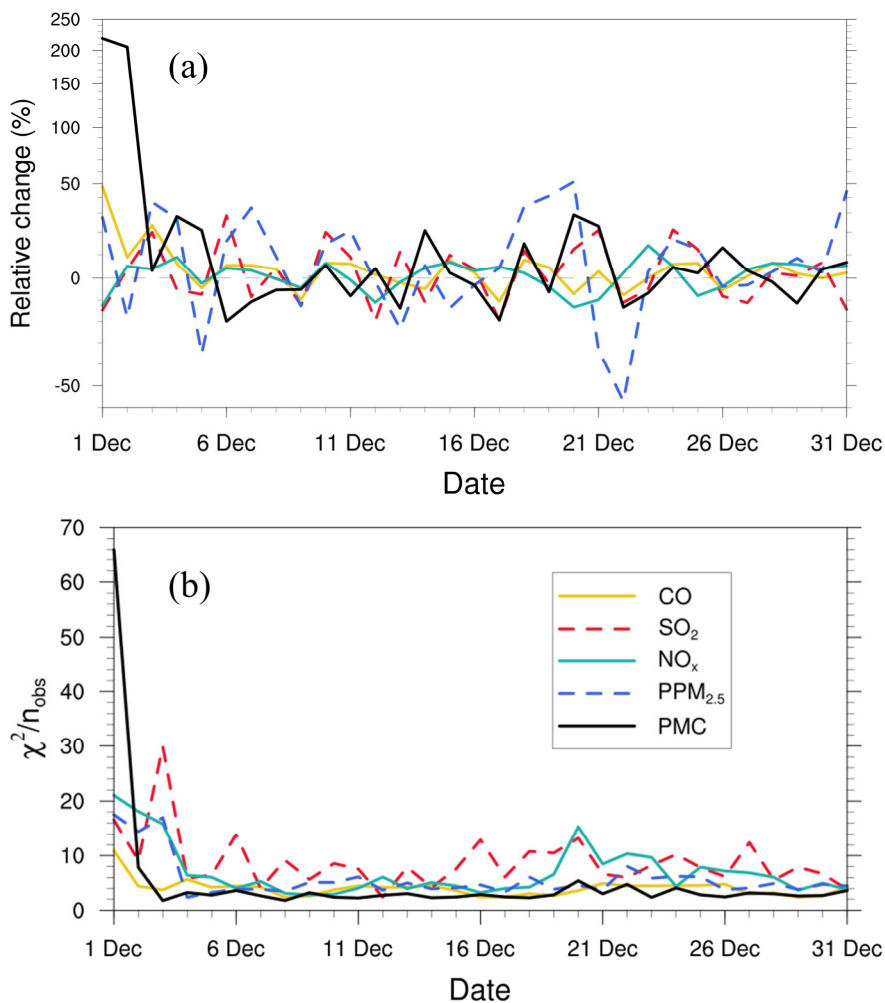
To diagnose the performance of the EnKF analysis, chi-squared (χ^2) statistics were calculated, which are generally used to test whether the prior ensemble mean RMSE

757 with respect to the observations is consistent with the prior “total spread” (square root
758 of the sum of ensemble variance and observation error variance). Following Zhang et
759 al. (2015), for the t th window, χ^2 is defined as:

$$760 \quad \chi_t^2 = (\mathbf{y} - \mathbf{H}\overline{\mathbf{X}^b})^T (\mathbf{H}\mathbf{P}^b\mathbf{H}^T + \mathbf{R})^{-1} (\mathbf{y} - \mathbf{H}\overline{\mathbf{X}^b}) \quad (20)$$

761 Figure 10.9 shows the time series of the relative changes between the prior and posterior
762 emissions and the χ^2 statistics. There were relatively large adjustments in emissions in
763 the first three windows, especially for the PMC. Subsequently, the five species reached
764 a more optimal state with successive emission inversion cycles. The χ^2 statistics showed
765 similar variation characteristics as the daily changes in emissions. The χ^2 value was
766 slightly greater than 1, indicating that the uncertainties from the error covariance
767 statistics did not fully account for the error in the ensemble simulations. A similar result
768 was reported by Chen et al. (2019). Further investigations should be conducted to
769 generate larger spreads by accounting for the influence of model errors. As we imposed
770 the same uncertainty of prior emissions at each DA window to partially compensate for
771 the influence of model errors, χ^2 statistics showed small fluctuations, indicating that the
772 system updated emissions consistently and stably.

773

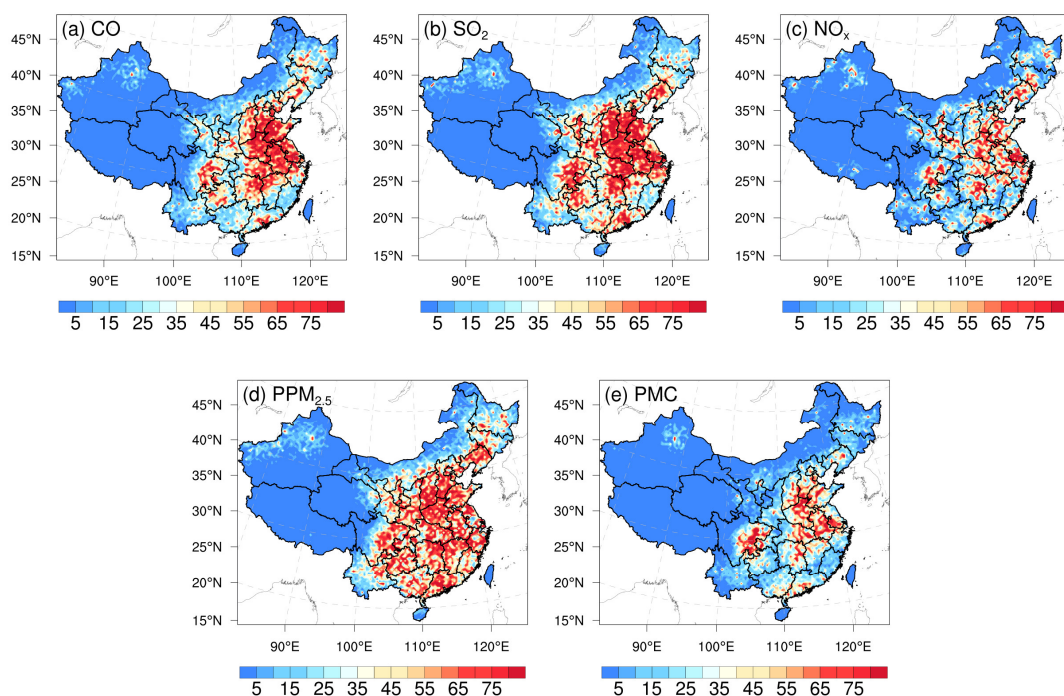


774

775 **Figure 109.** Relative changes (a) in posterior emission estimates of CO, SO₂, NO_x,
 776 PPM_{2.5}, and PMC and χ^2 statistics (b) of these state vectors in each window.

777 4.1.6 Evaluation using OSSE

778 Figure 104 shows the spatial distribution of the error reduction in the posterior
 779 emissions of the five species. After inversion, in most areas, the emission errors were
 780 reduced by more than 80%, especially in the central and eastern regions with dense
 781 observation sites, while in remote areas far away from cities, due to the sparse
 782 observation sites, the emission errors were still not well adjusted. Overall, the error
 783 reduction rates of CO, SO₂, NO_x, PPM_{2.5}, and PMC were 78.4%, 86.1%, 78.8%, 77.6%,
 784 and 72.0%, respectively, indicating that with the *in situ* observations in China, RAPAS
 785 can significantly reduce emission errors and thus showed good performance in emission
 786 estimates.



787

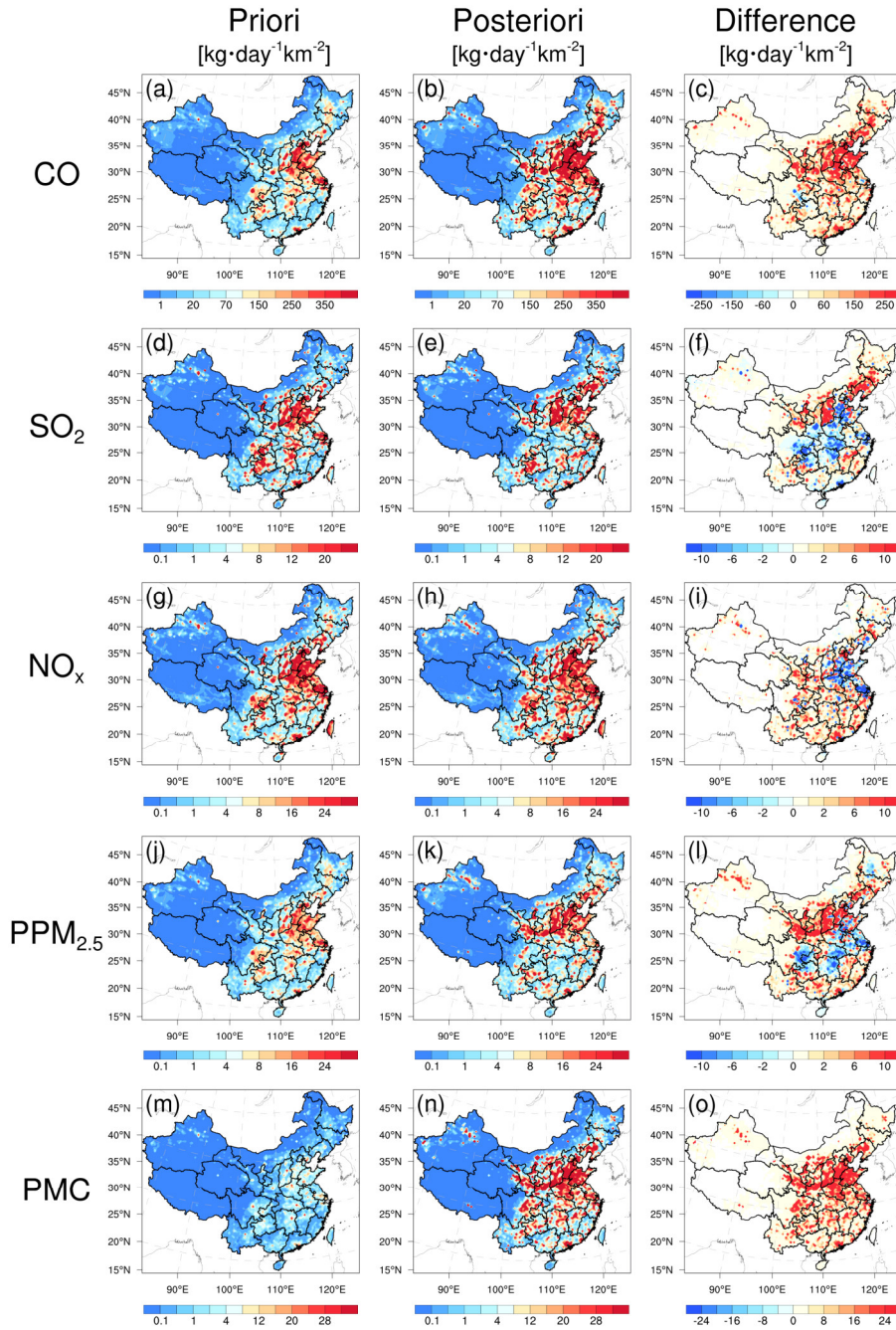
788 **Figure 10.1** Spatial distribution of the error reduction (%) of posterior emissions in the
 789 OSSE.

790 4.2 Inverted emissions

791 Figure 11.2 shows the spatial distribution of temporally averaged prior and posterior
 792 emissions and their differences in emissions in December 2016. It should be noted that
 793 emissions outside China were masked; as the observation sites were limited to China in
 794 this study, there was a slight change in the emissions outside China. Higher emissions
 795 were mainly concentrated in central and eastern China, especially in the NCP, YRD,
 796 and PRD, and lower emissions occurred across Northwest and Southern China.
 797 Compared with the prior emissions, posterior CO emissions were considerably
 798 increased across most areas of mainland China, especially in northern China, with an
 799 overall increase of 129%. A notable underestimation of prior emissions was also
 800 confirmed by inversion estimations (Feng et al., 2020b; Tang et al., 2013; Wu et al.,
 801 2020) and model evaluations (Kong et al., 2019b) in previous studies. For SO₂, the
 802 emissions increased mainly in Northeast China, Shanxi, Ningxia, Gansu, Fujian,
 803 Jiangxi, and Yunnan provinces. In SCB, Central China, YRD, and part of the NCP,

804 emissions were significantly reduced. The national total SO₂ emissions increased by
805 20%. For NO_x, although the increment of national total emissions was small
806 (approximately 5%), there were large deviations. The emissions in NCP and YRD were
807 reduced, whereas the emissions in most cities in other regions increased. The changes
808 in the emission of PPM_{2.5} were similar to those of SO₂. Compared with the prior
809 emissions, the posterior PPM_{2.5} emissions decreased over central China, SCB, and YRD,
810 whereas those in southern and northern China increased, especially in Shanxi, Shaanxi,
811 Gansu, and southern Hebei provinces. Overall, the relative increase was 95%. For PMC,
812 the posterior emissions were increased over all of mainland China, with national mean
813 relative increase exceeding 1000%. Larger emission increments mainly occurred in
814 areas with significant anthropogenic emissions of CO and PPM_{2.5}, indicating that the
815 large underestimation of PMC emissions in the prior inventory may be mainly
816 attributed to the underestimations of anthropogenic activities. The absence of natural
817 dust is another reason, as the wind-blown dust scheme was not applied in this study.
818 Overall, PM₁₀ emissions (PPM_{2.5}+PMC) increased by 318%. If we assume that all the
819 increments in PM₁₀ emissions are from natural dust, that means the contribution of
820 natural dust accounted for 75% of total PM₁₀ emissions, which is consistent with the
821 source apportionment of PM₁₀ of 75% in Changsha in Central China (Li et al., 2010).
822 Large PMC emission increments were also reported by Ma et al. (2019).

823 Detailed estimations of posterior emissions and relative changes compared to prior
824 emissions in each province and mainland China are given in Table S1. The evaluation
825 results for July showed that the emission uncertainty could still be significantly reduced
826 and the performance of the system in July was comparable to that in December (Table
827 S2). Additionally, the seasonal variation in emissions was well reflected (Figures S4
828 and S5), which means that our system performed well at different times of the year.
829 Note that the differences, excluding PMC, between the prior and posterior emissions
830 mainly reflect the deficiencies of the prior emissions as the times of the prior emissions
831 and observations were consistent in this study.



832

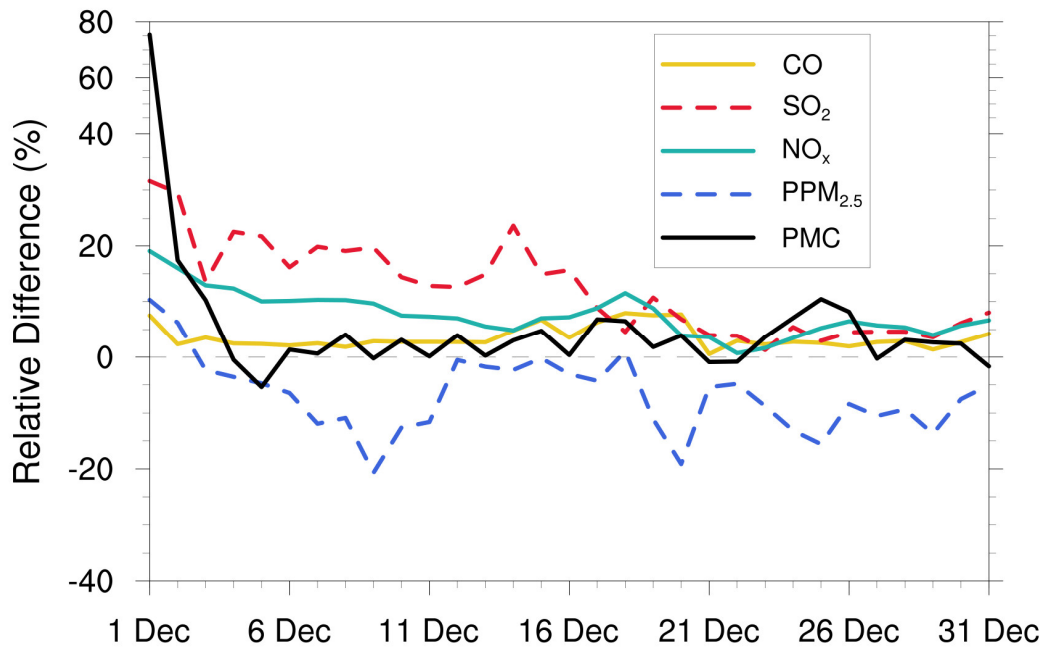
833 **Figure 112.** Spatial distribution of the time-averaged prior emissions (left column,
 834 MEIC 2016), posterior emissions (middle column), and differences (right column,
 835 posterior minus prior).

836 **4.3 Sensitivity tests**

837 **4.3.1 Impact of prior inventories**

838 Various prior inventories have shown considerable differences in space allocation and

839 emission magnitudes. Inversion results can be sensitive to a priori emissions if the
840 observations are insufficient (Gurney et al., 2004; He et al., 2018). MEIC 2012 was
841 used as an alternative a priori in EMS~~12~~ to investigate the impact of different prior
842 emissions on posterior emissions. Figure ~~123~~ shows the time series of the relative
843 differences in the daily posterior emissions of the five species between the EMDA (base)
844 and EMS~~12~~ experiments. Overall, the differences between the two posterior emissions
845 gradually decreased over time. At the beginning, the differences in the CO, SO₂, NO_x,
846 PPM_{2.5}, and PMC between the two inventories (i.e. MEIC 2012 vs. MEIC 2016) were
847 17.5%, 114.5%, 30.8%, 46.0%, and 72.0%, respectively, compared to 2.5%, 4.5%,
848 4.5%, -8.9%, and 3.0% in the last ten days. In addition, the species with larger emission
849 differences at the beginning took a longer time (i.e. more DA steps) to achieve
850 convergence. The quick convergence of PMC emissions was attributed to the large prior
851 uncertainty of 100% used in the first three DA windows. In contrast to the other species,
852 there were significant negative deviations in PPM_{2.5} emissions between the two
853 experiments. This may be due to the positive deviations in the precursors of PM_{2.5} (i.e.,
854 SO₂ and NO_x), which lead to a larger amount of secondary production. The PPM_{2.5}
855 emissions will be reduced to balance the total PM_{2.5}. We compared the PM_{2.5}
856 concentrations simulated by the two optimized inventories and found that they were
857 almost the same (Figure S6). Overall, this indicates that observations in China were
858 sufficient to infer emissions and that our system was robust. Meanwhile, the monthly
859 posterior emissions shown in Section 4.2 were still underestimated to a certain extent.



860

861 **Figure 123.** Relative differences in CO, SO₂, NO_x, PPM_{2.5}, and PMC emissions (% the
 862 ratio of absolute difference to EMDA) between the EMDA and EMS₁₂ experiments.

863

864 **4.3.2 Impact of prior uncertainties settings**

865 The uncertainty of prior emissions determines how closely the analysis is weighted
 866 towards the background and observations; however, information about prior
 867 uncertainties is generally not readily available. To evaluate the possible influence of
 868 prior uncertainties on the optimized emissions, we increased/reduced the uncertainties
 869 after three days of cycling, namely starting at 0000 UTC, 3 December, by 25% and 50 %
 870 in EMS₂₃ (-50%), EMS₃₄ (-25%), EMS₄₅ (+25%), and EMS₅₆ (+50%), respectively.

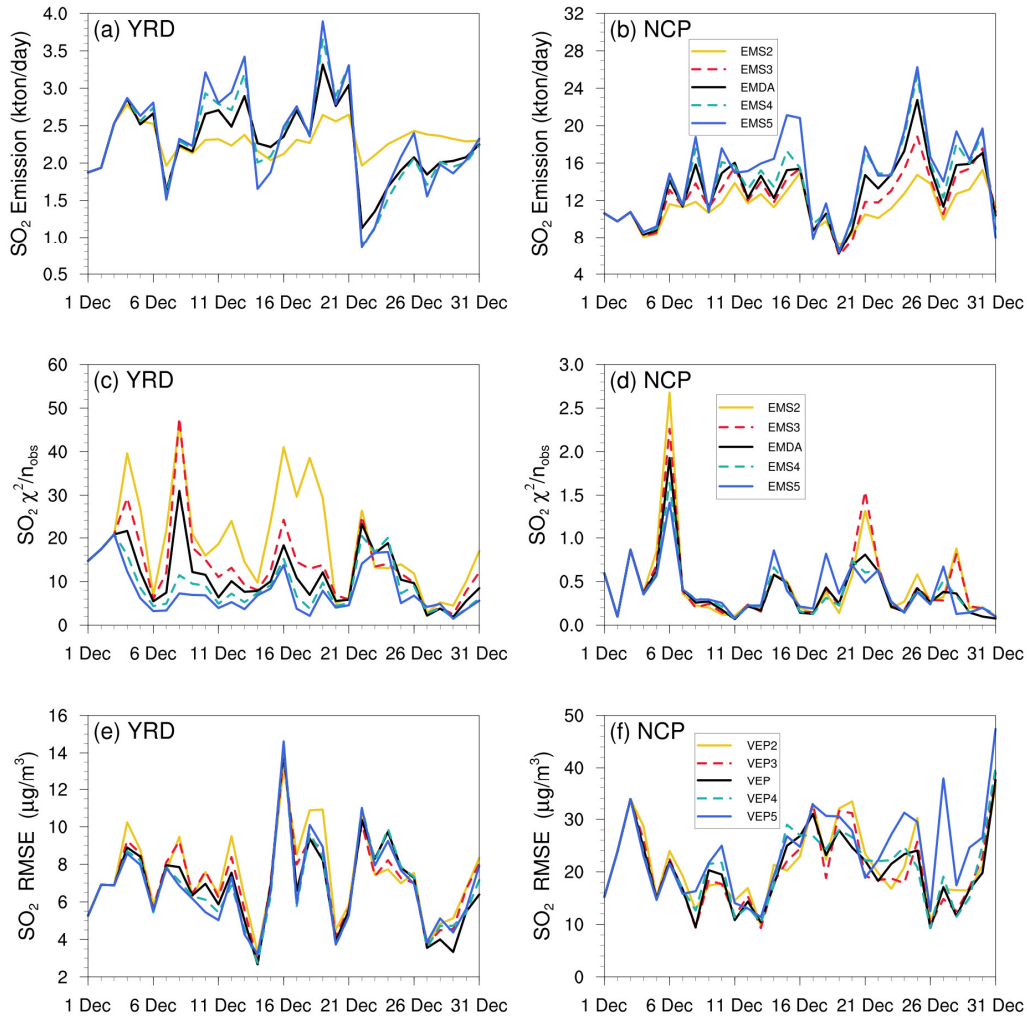
871 Table 87 summarizes the emission changes with different prior uncertainty settings in
 872 the EMS₂₃₋₅₆ experiments. To better understand the response of the system to the
 873 emission uncertainty settings, Figure 134 illustrates the time series of SO₂ emission
 874 changes, Chi-square statistics, and RMSEs of simulated SO₂ with emissions updated in
 875 the EMDA and EMS₂₃₋₅₆ experiments over the YRD and NCP (Figure 2). Compared
 876 with the EMDA, when the uncertainties decreased (increased), the emissions of the five
 877 species decreased (increased) accordingly. This is because the posterior emissions of
 878 the five species were larger than the prior emissions and, as shown in Figure 134a-d,

879 larger uncertainty will lead to faster convergence, resulting in larger posterior emissions.
 880 It can also be seen from Figure 134 that a faster convergence will reduce the RMSE of
 881 the simulated concentration with the posterior emissions in the early stage of the
 882 experiment; however, in the later stage of the experiment, there were no significant
 883 differences in the RMSE and Chi-square statistics among the different experiments.
 884 However, day-to-day changes in emissions also cause slight fluctuations. In addition,
 885 when greater uncertainties are set, the day-to-day changes in emissions are more drastic,
 886 resulting in a larger RMSE, as shown in the NCP. Moreover, the significant day-to-day
 887 variations in the estimated emissions may not be in line with the actual situation. Owing
 888 to the spatial-temporal inhomogeneity of emissions, the differences in Chi-square
 889 statistics between the YRD and NCP show that it may be necessary to apply different a
 890 priori uncertainties according to different regions (Chen et al., 2019). Therefore, when
 891 using an EnKF system for emission estimation, error setting must be carefully executed.
 892 Overall, the uncertainties chosen in EMDA aim to minimize the deviation of the
 893 concentration fields and maintain the stability of the inversion.

894 **Table 87.** Relative differences in CO, SO₂, NO_x, PPM_{2.5} and PMC emissions (% the
 895 ratio of absolute difference to EMDA) between the EMDA and EMS~~23~~-~~56~~ experiments.

| Species | EMS 23 | EMS 34 | EMS 45 | EMS 56 |
|--------------------|-------------------|-------------------|-------------------|-------------------|
| CO | -8.6 | -4 | 3 | 5.2 |
| SO ₂ | -14 | -5.7 | 3.6 | 6.8 |
| NO _x | -6.5 | -3 | 2.8 | 4.5 |
| PPM _{2.5} | -16.5 | -7.8 | 4.6 | 8.7 |
| PMC | -18.5 | -8.2 | 7.3 | 13.1 |

896



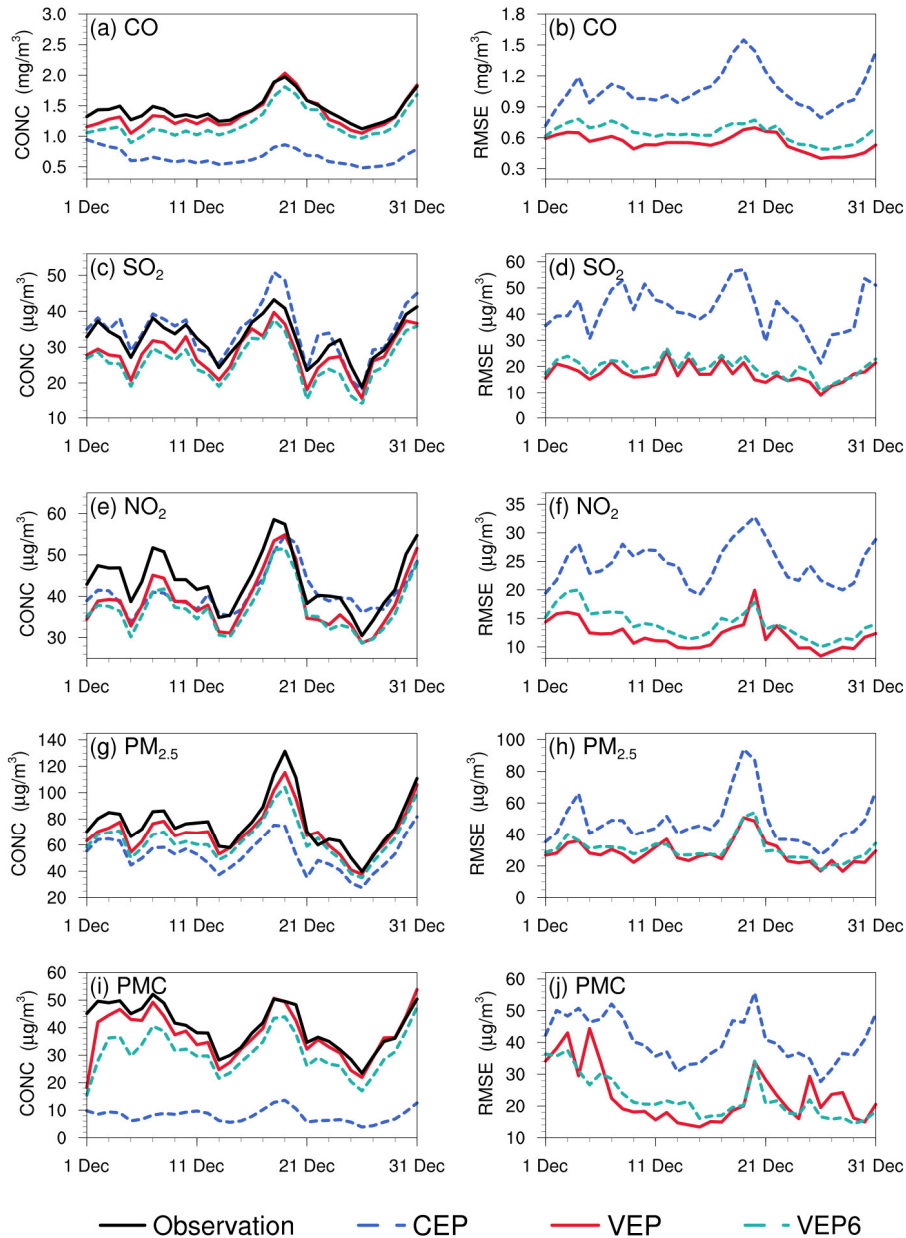
897

898 **Figure 134.** Time-series of SO₂ emission changes, Chi-square statistics, and RMSE of
 899 simulated SO₂ with updated SO₂ emissions in the EMDA and EMS₂₃₋₅₆ experiments
 900 over the YRD and NCP.

901 **4.3.3 Impact of observation error settings**

902 Observation errors are another factor that determine the relative weights of the
 903 observations and background in the analysis. A proper estimate of the observation error
 904 is important for filter performance; however, observation errors are generally not
 905 provided with datasets. The observation error is usually set to a fixed value (Ma et al.,
 906 2019), specific proportion of the observation value (Tang et al., 2013), or value
 907 calculated by combining measurement error with representative error as used in this
 908 study. Generally, the performance of data assimilation is sensitive to the specification

909 of the observation error (Tang et al., 2013). Sensitivity experiment (EMS~~67~~) with
910 doubled observation error was conducted to evaluate the influence of observation error
911 on the optimized emissions. Overall, the spatial distribution of emissions after
912 optimization was almost the same as that of the EMDA experiment but with a lower
913 increment (Figure S7), resulting in a weaker estimate of the national total emissions for
914 each species. This is because that the observation error inflates and the system becomes
915 more certain of the prior emission, and reduces the effect of observation information.
916 Figure 1~~45~~ shows the time series of simulated and observed daily concentrations and
917 their RMSEs verified against the assimilated sites. The simulations in VEP~~67~~ usually
918 performed worse, with larger biases and RMSEs than those of VEP (Figures S8 and S9),
919 especially in western and southern China, where posterior emissions were significantly
920 underestimated. These results generally corresponded to sluggish emission changes and
921 large Chi-square statistics (Figure S10), suggesting that an observation error that is too
922 large may substantially impact the estimated emissions.



923

924

925

926

Figure 145. Time series of the daily concentrations (CONC, left) and root mean square error (RMSE, right) obtained from CEP, VEP, ~~VEP1~~, and VEP7. The simulations were verified against the assimilated sites.

927

4.3.4 Impact of the IC optimization of the first window

928

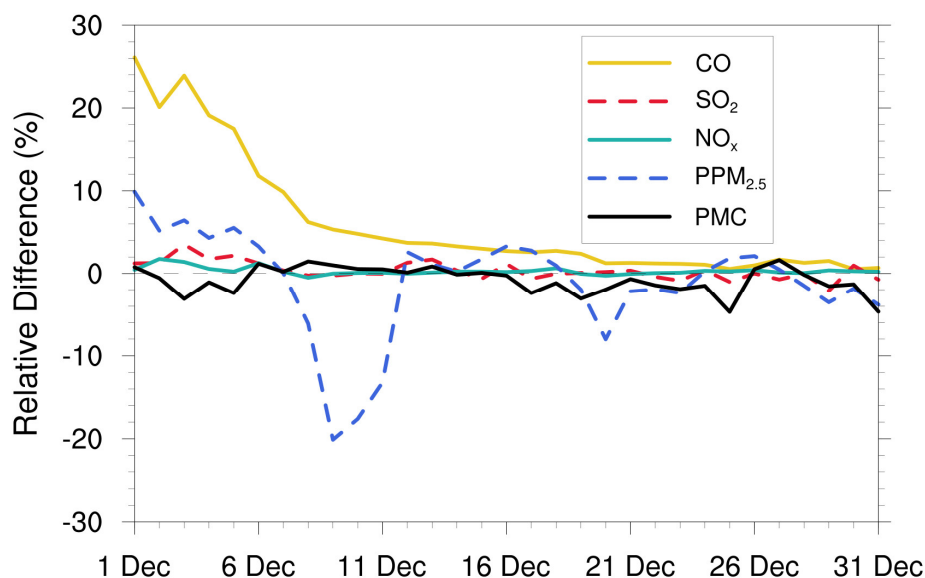
929

930

931

Several studies indicate large emission discrepancies resulting from IC errors (Jiang et al., 2013a; Miyazaki et al., 2017; Tang et al., 2013), which means that if the IC is not optimized, the errors of concentrations would be compensated for through the adjustment of emissions. To evaluate the impact of IC optimization of the first window

932 on the emission inversions, an EMS78 experiment without the IA step was conducted.
 933 Figure 156 shows the time series of the relative differences in the daily posterior
 934 emissions of the five species between the EMDA and EMS78 experiments. It can be
 935 observed that IC optimization had a significant impact on the emission inversions of
 936 long-lived species (i.e. CO). The overall difference in the inverted CO emissions
 937 between the two experiments was approximately 5.3% but can reach 26.1% in the first
 938 few windows. For the short-lived species, IC optimization had little impact on the
 939 emissions; for example, the average emission differences of SO₂, NO_x, and PMC in the
 940 two experiments were 0.3%, 0.3%, and 0.9%, respectively. For PPM_{2.5}, the average
 941 emission difference is affected not only by primary emissions, but also by the complex
 942 chemistry of its precursors. Therefore, the difference between the two experiments
 943 fluctuated, with overall difference of 2%. Notably, with the gradual disappearance of
 944 the benefit of IC assimilation, the two experiments reached a unified state after several
 945 windows. For CO, the impact of IA on emission inversion lasted approximately half a
 946 month. These results indicate that removing the bias of the IC of the first DA window
 947 is essential for the subsequent inverse analysis (Jiang et al., 2017).



948

949 **Figure 156.** Relative differences in CO, SO₂, NO_x, PPM_{2.5}, and PMC emissions (% the
 950 ratio of absolute difference to EMDA) between the EMDA and EMS78.

4.3.5 Advantages of the “two-step” scheme

Adjusting the ICs and emissions simultaneously (“one-step” scheme) has been applied to constrain prior emissions in previous studies (e.g., Evensen, 2009; Kong et al., 2019a). To investigate the impact of different methods on the optimized emissions, a sensitivity test (EMS1) was performed, in which the ICs of each DA window were also optimized using the EnSRF algorithm (Peng et al., 2018; Schwartz et al., 2014). The spatial localization radius for updating ICs was set to 90 km in horizontal and 5 layers in vertical closet to the surface with better vertical mixings. The selections of the horizontal and vertical scales were similar to Kong et al. (2021) and Tang et al. (2016). We evaluated the optimized ICs of each step, and the results showed that IC assimilation with EnSRF had good performance (Figure S11).

Compared with our “two-step” method (EMDA), the posterior emissions of EMS1 were 7.9%, 9.6%, 2.7%, 27.1%, and 22.8% higher for CO, SO₂, NO_x, PPM_{2.5}, and PMC, respectively (Figure S12). The higher emission increase was mainly distributed in the northern China (Figure S13). We also evaluated the posterior emissions of EMS1 (VEP1) using the method described in Section 4.1.3. Overall, compared with EMDA, the performance of EMS1 was worse, with RMSEs of CO, SO₂, NO₂, PM_{2.5} and PMC increasing from 0.56 mg m⁻³ and 17.7, 12.3, 29.6, and 24.6 μg m⁻³ to 0.58 mg m⁻³ and 18.3, 12.9, 34.9, and 25.9 μg m⁻³, respectively (Figure 15). From the perspective of spatial distribution, the evaluation results become worse in areas where emissions increase (Figure S13). Additionally, it can be seen from the Figure 15 that the results of the VEP and VEP1 were relatively close at the beginning. However, in the heavy pollution (16–21 December) and later period, the VEP1 with “one-step” inversion emissions had higher concentrations than the observations and larger RMSE than VEP. The results verified against the independent sites showed a similar situation (Figure S8). This may be because during the period of heavy pollution, the WRF/CMAQ (offline model) did not consider the feedback process of meteorology and chemistry, resulting in low simulated values. Therefore, the system compensates for the underestimated concentrations caused by the model error through more emissions, resulting in an

980 ~~overestimation of emissions. The accumulation of emission errors in each independent~~
981 ~~window further leads to the overestimation of concentration after the end of high~~
982 ~~pollution, especially for species with a long lifetime (e.g. CO). In contrast, using the~~
983 ~~“two-step” inversion scheme, this overestimation will be corrected quickly in the~~
984 ~~subsequent inversion to ensure the stability of the system.~~

985 ~~As mentioned previously, in the “two-step” scheme, the unresolved posterior emission~~
986 ~~error is fed back to the IC of the next window through a sufficient mixed simulation~~
987 ~~within one day for timely optimization. Meanwhile, the system maintains the mass~~
988 ~~balance of the pollutants. Thus, the system updates emissions more consistently and~~
989 ~~stably. If the emission in one window is overestimated, it can be compensated for in the~~
990 ~~next window with lower estimates. In contrast, when the ICs are optimized~~
991 ~~simultaneously at each window, the overestimation will not be corrected and will~~
992 ~~accumulate to the end (Figure S14). In addition, the assimilation for initial fields cannot~~
993 ~~be perfect (Figure S11). As shown in Figure S14, during the heavy pollution episode,~~
994 ~~there were negative biases in the optimized ICs every day, which lead to a larger~~
995 ~~positive and a smaller negative emission increment at a certain extent, and result in a~~
996 ~~larger emission in the end.~~

997 ~~To remove the effect of this imperfect initial field, we conducted another OSSE~~
998 ~~experiment (OSSE_TRUEIC) using “one step” scheme, in which the IC of each~~
999 ~~window was directly taken from the “true” simulation. We further compared the~~
1000 ~~emission error reductions between the OSSE experiment (Section 3) and the~~
1001 ~~OSSE_TRUEIC experiment. The results showed that during the last ten days, the error~~
1002 ~~reductions of OSSE_TRUEIC were 70.7%, 78.6%, 73.3%, 72.4%, and 63.6% for CO,~~
1003 ~~SO₂, NO_x, PPM_{2.5}, and PMC, respectively, which were smaller than those in the OSSE~~
1004 ~~experiment (Section 4.1.6, Figure S15), indicating that even with a perfect IC at each~~
1005 ~~window, the inversion performance of “one-step” scheme was still not as good as that~~
1006 ~~of the “two-step” method.~~

1007 ~~Additionally, as shown in section 4.3.1, with the “two-step” scheme, the differences of~~

1008 ~~emissions inverted using MEIC 2012 and 2016 as a priori were only 2.5%, 4.5%, 4.5%,~~
1009 ~~-8.9%, and 3.0% for CO, SO₂, NO_x, PPM_{2.5} and PMC, respectively in the last ten days.~~
1010 ~~We further tested the convergence of the posterior emissions in the "one-step" inversion.~~
1011 ~~Except for PPM_{2.5}, the relative differences of other species in posterior emissions were~~
1012 ~~slightly larger than that between EMDA and EMS2 with the "two-step" scheme (Figure~~
1013 ~~S16), which further underscores the advantages of the "two-step" scheme. It should be~~
1014 ~~noted that model performance depends on many factors but does not affect the~~
1015 ~~advantage of the "two-step" scheme in emission inversion.~~

1016 **4.4 Discussion**

1017 Optimal state estimation using an EnKF relies on the assumption of an unbiased
1018 Gaussian prior error, which is not guaranteed in such highly nonlinear and large bias
1019 systems. In this study, some pollutants (e.g. CO, PMC) have very large simulated biases;
1020 thus, if a small uncertainty is adopted, the emission bias cannot be fully reduced. If a
1021 very large uncertainty is adopted, then the degree of freedom of adjustment is too large
1022 and the inverted daily emissions will fluctuate abnormally. Therefore, we only set a
1023 larger prior uncertainty in the first three windows, adopting a moderate uncertainty in
1024 the following windows and used a "two-step" inversion scheme and cyclic iteration to
1025 gradually correct the emission errors. Figure ~~9a10(a)~~ shows the time series of the
1026 relative differences between prior and posterior emissions in each window. There were
1027 relatively large adjustments for the emissions in the first three windows, especially for
1028 PMC, but the adjustment ranges of the five species after the first three windows were
1029 within the uncertainty range (e.g. $\pm 25\%$), indicating that with this scheme, the EnKF
1030 method used in this system had a good performance in emission inversion.

1031 Model-data mismatch errors are from both the emissions and the inherent model errors
1032 arising from the model structure, discretization, parameterizations, and biases in the
1033 simulated meteorological fields. Neglecting model errors would attribute all
1034 uncertainties to emissions and lead to considerable bias in the estimated emissions. In
1035 the version of the CMAQ model used in this study, there are no heterogeneous reactions

1036 (Quan et al., 2015; Wang et al., 2017), the parameterization scheme for the formation
1037 of secondary organic aerosols (SOA) is imperfect (Carlton et al., 2008; Jiang et al.,
1038 2012; Yang et al., 2019), no feedback between chemistry and meteorology was
1039 considered, and we used an idea profile for chemical lateral boundary conditions. All
1040 the above problems can lead to underestimated concentrations of pollutants, which in
1041 turn require more emissions to compensate, leading to overestimation of emissions. In
1042 addition, previous studies showed that ammonia emissions in the MEIC inventory are
1043 underestimated (Kong et al., 2019b; Paulot et al., 2014; Zhang et al., 2018). Owing to
1044 lack of ammonia observations, our system does not include emission estimates of
1045 ammonia, which means that the concentration of ammonium aerosol was
1046 underestimated in this system, also resulting in an overestimation of the $\text{PPM}_{2.5}$
1047 emission. Wind-blown dust was also not simulated; thus, the PMC emission inverted in
1048 this system come from anthropogenic activities and natural sources. Although some of
1049 these shortcomings can be solved by updating the CTM model, there will still be errors
1050 in each parameterization and process. In general, a parameter estimation method was
1051 used to reduce the model errors, in which some uncertain parameters were included in
1052 the augmented state vector and optimized synchronously based on the available
1053 observations (Brandhorst et al., 2017; Evensen, 2009). However, it is difficult to
1054 identify the key uncertain parameters of different species in different models, which
1055 generally comes not only from the complex atmospheric chemical model but also from
1056 hundreds of model inputs (Tang et al., 2013). Another method is bias correction, which
1057 treats the model error as a bias term and includes it in an augmented state vector
1058 (Brandhorst et al., 2017; De Lannoy et al., 2007; Keppenne et al., 2005). In addition,
1059 the weak-constraint 4DVAR method can be used to reduce model errors, which adds a
1060 correction term in the model integration to account for the different sources of model
1061 error (Sasaki, 1970). Although the reliable diagnosis of model error remains a challenge
1062 (Laloyaux et al., 2020), it should be considered in an assimilation system. In the future,
1063 we will consider model errors in our system to obtain better emission estimates.

1064 Independent variable localization was adopted to avoid potential spurious correlations

1065 across different species in this study. However, the transmission scales for different
1066 species in different regions differ, and a more accurate localization range can be
1067 obtained through backward trajectory analysis. In addition, O₃ observations were not
1068 assimilated to improve NO_x and VOC emissions using cross-species information. O₃
1069 concentration and NO_x (VOC) emissions were positively correlated in the NO_x (VOC)-
1070 limited region and negatively correlated in the VOC (NO_x)-limited region (Tang et al.,
1071 2011; Wang et al., 2019b). Hamer et al. (2015) successfully used O₃ observations to
1072 estimate NO_x and VOC emissions within the 4DVAR framework within an ideal model.
1073 However, the NO_x emissions are often point or line sources, which are all small
1074 compared to the model resolution. With a coarse spatial resolution, the model cannot
1075 accurately simulate the relationships between O₃ and its precursors. When assimilating
1076 O₃ observations to infer NO_x or VOC emissions, the inaccurate relationships simulated
1077 by model would worsen the inversion of NO_x emissions (Inness et al., 2015). In general,
1078 improving the model resolution can improve the detailed simulation and provide better
1079 prior information on O₃-NO_x-VOC, but it is still difficult to determine whether the
1080 condition is NO_x-limited or VOC-limited in the real atmosphere using prior emissions
1081 (Liu and Shi, 2021). Elbern et al. (2007) emphasized that assimilating O₃ to correct NO_x
1082 or VOC emissions must follow the EKMA framework derived based on observations,
1083 otherwise, even if the resolution is improved to sufficiently solve point and line sources,
1084 precursor emissions may be still adjusted in an opposite direction. This can be
1085 demonstrated in our OSSE experiment at high resolution of 3 km (Figure S11). In this
1086 study, the spatial resolutions of the prior emission inventory (i.e., MEIC) is 0.25° ×
1087 0.25°, which is appropriate for modeling at regional scales (Zheng et al., 2017). With
1088 this emission inventory, it is unable to accurately simulate the O₃-NO_x-VOC
1089 relationships. Therefore, to avoid the impact of inaccurate O₃-NO_x relationship on
1090 emission inversion, in our system, we did not assimilate O₃, but directly assimilate NO₂
1091 to optimize the NO_x emissions. This work will be followed by an ongoing study using
1092 the available VOC observations.

1093 Although we do not assimilate O₃ observation, model resolution still has some influence

1094 on inversion results. In our previous study (Feng et al., 2022), we have inferred the NO_x
1095 emissions over YRD in China using NO₂ observations, which has a spatial resolution
1096 of 12 km. The study period, assimilated observations, and inversion settings are the
1097 same as this study. We compared the posterior emissions of YRD between this study
1098 and Feng et al. (2022). The results showed that there was similar spatial distribution of
1099 posterior emissions inferred using the two resolutions (36 km vs 12 km) (Figure
1100 [R17S12](#)), but the total NO_x emission in YRD inferred using 36 km resolution was about
1101 8.8% higher than that inferred using 12 km resolution. The differences are mainly
1102 caused by meteorological differences at different resolutions. This indicates that coarse
1103 model resolution may lead to some overestimation of the inverted emissions. In addition,
1104 as shown previously, the concentrations after DA were evidently underestimated in
1105 western China, indicating that the inverted emissions over these regions still have large
1106 uncertainties because of the sparsity of observations, which are spatially insufficient for
1107 sampling the inhomogeneity of emissions. Therefore, further investigations with the
1108 joint assimilation of multisource observations (e.g. satellite) are underway.

1109 NO_x is mainly emitted by transportation (Li et al., 2017), which can reflect the level of
1110 economic activity to a certain extent. Weekly emission changes were explored to verify
1111 the performance of the system in depicting emission changes (Figure [S138](#)). Although
1112 the “weekend effect” of emissions in China is not significant (Wang et al., 2014; Wang
1113 et al., 2015), the posterior NO_x emission changes are in good agreement with the
1114 observations. In our previous studies (Feng et al., 2020a; Feng et al., 2020b), this system
1115 was successfully applied to optimize NO_x and CO emissions. The inverted emission
1116 changes were also in line with the epidemic control time points. Additionally, the
1117 emission changes can reflect the emission migration from developed or urban areas to
1118 developing or surrounding areas in recent years, which is consistent with the emission
1119 control strategies in China. Although the system did not consider the model error,
1120 resulting in a certain difference between the posterior and actual emissions, the
1121 spatiotemporal changes in posterior emissions were relatively reasonable and can be
1122 used to monitor emission changes and inform emission regulations.

1123 **5 Summary and conclusions**

1124 In this study, we developed a Regional multi-Air Pollutant Assimilation System
1125 (RAPASv1.0) based on the WRF/CMAQ model, 3DVAR algorithm, and EnKF
1126 algorithm. RAPAS can quantitatively optimize gridded emissions of CO, SO₂, NO_x,
1127 PPM_{2.5}, and PMC on a regional scale by simultaneously assimilating hourly *in situ*
1128 measurements of CO, SO₂, NO₂, PM_{2.5}, and PM₁₀. This system includes two subsystems:
1129 IA subsystem and EI subsystem, which optimize chemical ICs and infer anthropogenic
1130 emissions.

1131 Taking the 2016 MEIC in December as a priori, the emissions of CO, SO₂, NO_x, PPM_{2.5},
1132 and PMC in December 2016 were inferred by assimilating the corresponding
1133 nationwide observations over China. The optimized ICs and posterior emissions were
1134 examined against assimilated and independent observations through parallel forward
1135 simulation experiments with and without DA. Sensitivity tests were performed to
1136 investigate the impact of different inversion processes, prior emissions, prior
1137 uncertainties, and observation errors on emission estimates.

1138 RAPAS showed a good performance in assimilating surface *in situ* observations, with
1139 the calculated emission uncertainties reduced by 44.4%, 45.0%, 34.3%, 51.8%, and
1140 56.1% for CO, SO₂, NO_x, PPM_{2.5}, and PMC, respectively. It can also significantly
1141 improve the simulations; the RMSEs of the simulated concentrations with posterior
1142 emissions decreased by 40.1–56.3% and the CORRs increased from 0.26–0.66 to 0.69–
1143 0.87 for different species. The OSSE experiment showed that the errors of posterior CO,
1144 SO₂, NO_x, PPM_{2.5}, and PMC could be reduced by 78.4%, 86.1%, 78.8%, 77.6%, and
1145 72.0%, respectively. Overall, compared with the prior emissions (MEIC 2016), the
1146 posterior emissions increased by 129%, 20%, 5%, and 95% for CO, SO₂, NO_x, and
1147 PPM_{2.5}, respectively. The posterior PMC emissions, which included anthropogenic and
1148 natural dust contributions, increased by 1045%. ~~Sensitivity tests with different
1149 inversion processes revealed that the “two step” scheme outperformed the joint
1150 adjustment of ICs and emissions (“one step” scheme) in emission inversion, especially~~

1151 ~~after heavy pollution.~~ Sensitivity tests with different prior inventories showed that the
1152 observations in China were sufficient to infer emission and that our system was less
1153 dependent on prior inventories. Additionally, sensitivity tests with different prior
1154 uncertainties indicated that when the posterior emissions were larger than the prior
1155 emissions, the emissions decreased/increased with decreases/increases in uncertainties
1156 because of the different convergence rates. These results demonstrate the advantage of
1157 the two-step method in emission inversion in that the inversion errors of the last window
1158 can be transferred to the current window for further optimization and robustness of the
1159 emissions estimated from RAPAS using nationwide observations over China. It should
1160 be noted that the system usually responds slowly to too small a priori uncertainties or
1161 too large observation errors, which may result in large errors in the estimated emissions.

1162 In summary, the comprehensive evaluation and sensitivity tests revealed that RAPAS
1163 could serve as a useful tool for accurately quantifying the spatial and temporal changes
1164 in multi-species emissions at regional scales and near-real time, which will be helpful
1165 for air pollution control in China and other regions around the world with dense ground
1166 observation networks.

1167

1168

1169

1170

1171

1172

1173

1174

1175

1176

1177 **Code and data availability**

1178 The codes of RAPAS v1.0 are available at <https://doi.org/10.5281/zenodo.5566225>.
1179 The WRF model code is open-source code and can be obtained from the WRF Model
1180 User's Page (<https://www2.mmm.ucar.edu/wrf/users>, last access: 25 April 2021). The
1181 CMAQ model is available through an open license as well (<https://www.epa.gov/cmaq>,
1182 last access: 25 April 2021). The observational and emission data used in this study are
1183 available at <https://doi.org/10.5281/zenodo.4718290> (Feng and Jiang, 2021).

1184

1185 **Author contribution**

1186 SF, FJ, ZW and ZJ developed RAPAS v1.0. SF and FJ designed the research. SF
1187 performed model simulations, analyzed data, and prepared the paper with contributions
1188 from all co-authors. FJ supervised the model development project and assisted in
1189 conceptualization and writing. HW, WH, YS, LZ, YZ, CL, and WJ contributed to the
1190 discussion and improvement of the paper.

1191

1192 **Competing interests**

1193 The authors declare that they have no conflict of interest.

1194

1195 **Acknowledgements**

1196 This work is supported by the National Key R&D Program of China (Grant No.
1197 2020YFA0607504), the National Natural Science Foundation of China (Grant No.
1198 41907378), and the Nanjing University Innovation and Creative Program for Ph.D.
1199 candidate (Grant No. CXCY19-60). We are grateful to the High Performance
1200 Computing Center (HPCC) of Nanjing University for doing the numerical calculations
1201 in this paper on its blade cluster system, and thank the MEIC team for providing the
1202 prior anthropogenic emissions (<http://www.meicmodel.org/>).

1203 **References**

- 1204 Appel, K. W., Pouliot, G. A., Simon, H., Sarwar, G., Pye, H. O. T., Napelenok, S. L., Akhtar, F., and
1205 Roselle, S. J.: Evaluation of dust and trace metal estimates from the Community Multiscale Air
1206 Quality (CMAQ) model version 5.0, *Geoscientific Model Development*, 6, 883-899,
1207 10.5194/gmd-6-883-2013, 2013.
- 1208 Alexe, M., Bergamaschi, P., Segers, A., Detmers, R., Butz, A., Hasekamp, O., Guerlet, S., Parker,
1209 R., Boesch, H., Frankenberg, C., Scheepmaker, R. A., Dlugokencky, E., Sweeney, C., Wofsy,
1210 S. C., and Kort, E. A.: Inverse modelling of CH₄ emissions for 2010-2011 using different
1211 satellite retrieval products from GOSAT and SCIAMACHY, *Atmospheric Chemistry and
1212 Physics*, 15, 113-133, 2015.
- 1213 Barbu, A. L., Segers, A. J., Schaap, M., Heemink, A. W., and Bultjes, P. J. H.: A multi-component
1214 data assimilation experiment directed to sulphur dioxide and sulphate over Europe,
1215 *Atmospheric Environment*, 43, 1622-1631, 2009.
- 1216 Bocquet, M.: Parameter-field estimation for atmospheric dispersion: application to the Chernobyl
1217 accident using 4D-Var, *Quarterly Journal of the Royal Meteorological Society*, 138, 664-681,
1218 2012.
- 1219 Bocquet, M., Elbern, H., Eskes, H., Hirtl, M., Žabkar, R., Carmichael, G. R., Flemming, J., Inness,
1220 A., Pagowski, M., Pérez Camaño, J. L., Saide, P. E., San Jose, R., Sofiev, M., Vira, J., Baklanov,
1221 A., Carnevale, C., Grell, G., and Seigneur, C.: Data assimilation in atmospheric chemistry
1222 models: current status and future prospects for coupled chemistry meteorology models,
1223 *Atmospheric Chemistry and Physics*, 15, 5325-5358, 2015.
- 1224 Bocquet, M. and Sakov, P.: Joint state and parameter estimation with an iterative ensemble Kalman
1225 smoother, *Nonlinear Processes in Geophysics*, 20, 803-818, 2013.
- 1226 Basu, S., Guerlet, S., Butz, A., Houweling, S., Hasekamp, O., Aben, I., Krummel, P., Steele, P.,
1227 Langenfelds, R., Torn, M., Biraud, S., Stephens, B., Andrews, A., and Worthy, D.: Global CO₂
1228 fluxes estimated from GOSAT retrievals of total column CO₂, *Atmospheric Chemistry and
1229 Physics*, 13, 8695-8717, 2013.
- 1230 Bauwens, M., Compernelle, S., Stavrou, T., Müller, J.-F., van Gent, J., Eskes, H., Levelt, P. F.,
1231 van der A, R., Veefkind, J. P., Vlietinck, J., Yu, H., and Zehner, C.: Impact of Coronavirus
1232 Outbreak on NO₂ Pollution Assessed Using TROPOMI and OMI Observations, 47,
1233 e2020GL087978, 10.1029/2020gl087978, 2020.
- 1234 Bierman: Factorization methods for Discrete Sequential estimation, Academic Press, 1977.
- 1235 Binkowski, F. S. and Roselle, S. J.: Models-3 community multiscale air quality (CMAQ) model
1236 aerosol component - 1. Model description, *Journal of Geophysical Research-Atmospheres*, 108,
1237 10.1029/2001jd001409, 2003.
- 1238 Brandhorst, N., Erdal, D., and Neuweiler, I.: Soil moisture prediction with the ensemble Kalman
1239 filter: Handling uncertainty of soil hydraulic parameters, *Advances in Water Resources*, 110,
1240 360-370, 2017.

- 1241 Bruhwiler, L. M. P., Michalak, A. M., Peters, W., Baker, D. F., and Tans, P.: An improved Kalman
1242 Smoother for atmospheric inversions, *Atmos. Chem. Phys.*, 5, 2691-2702, 10.5194/acp-5-
1243 2691-2005, 2005.
- 1244 Carlton, A. G., Turpin, B. J., Altieri, K. E., Seitzinger, S. P., Mathur, R., Roselle, S. J., and Weber,
1245 R. J.: CMAQ Model Performance Enhanced When In-Cloud Secondary Organic Aerosol is
1246 Included: Comparisons of Organic Carbon Predictions with Measurements, *Environmental
1247 Science & Technology*, 42, 8798-8802, 2008
- 1248 Chen, D., Liu, Z., Ban, J., and Chen, M.: The 2015 and 2016 wintertime air pollution in China: SO₂
1249 emission changes derived from a WRF-Chem/EnKF coupled data assimilation system,
1250 *Atmospheric Chemistry and Physics*, 19, 8619-8650, 10.5194/acp-19-8619-2019, 2019.
- 1251 Chen, D., Liu, Z., Fast, J., and Ban, J.: Simulations of sulfate-nitrate-ammonium (SNA) aerosols
1252 during the extreme haze events over northern China in October 2014, *Atmospheric Chemistry
1253 and Physics*, 16, 10707-10724, 10.5194/acp-16-10707-2016, 2016.
- 1254 Chevallier, F., Bréon, F.-M., and Rayner, P. J.: Contribution of the Orbiting Carbon Observatory to
1255 the estimation of CO₂ sources and sinks: Theoretical study in a variational data assimilation
1256 framework, 112, 10.1029/2006JD007375, 2007.
- 1257 Clements, A. L., Fraser, M. P., Upadhyay, N., Herckes, P., Sundblom, M., Lantz, J., and Solomon,
1258 P. A.: Chemical characterization of coarse particulate matter in the Desert Southwest - Pinal
1259 County Arizona, USA, *Atmospheric Pollution Research*, 5, 52-61, 10.5094/apr.2014.007, 2014.
- 1260 Clements, N., Hannigan, M. P., Miller, S. L., Peel, J. L., and Milford, J. B.: Comparisons of urban
1261 and rural PM_{10-2.5} and PM_{2.5} mass concentrations and semi-volatile fractions in northeastern
1262 Colorado, *Atmospheric Chemistry and Physics*, 16, 7469-7484, 10.5194/acp-16-7469-2016,
1263 2016.
- 1264 Daley, R.: Atmospheric Data Assimilation (gtSpecial Issue>Data Assimilation in Meteorology and
1265 Oceanography: Theory and Practice), *Journal of the Meteorological Society of Japan. Ser. II*,
1266 75, 319-329, 1997.
- 1267 Derber, J. C.: A VARIATIONAL CONTINUOUS ASSIMILATION TECHNIQUE, *Monthly
1268 Weather Review*, 117, 2437-2446, 1989.
- 1269 de Foy, B., Lu, Z., Streets, D. G., Lamsal, L. N., and Duncan, B. N.: Estimates of power plant NO_x
1270 emissions and lifetimes from OMI NO₂ satellite retrievals, *Atmospheric Environment*, 116, 1-
1271 11, 10.1016/j.atmosenv.2015.05.056, 2015.
- 1272 De Lannoy, G. J. M., Houser, P. R., Pauwels, V. R. N., and Verhoest, N. E. C.: State and bias
1273 estimation for soil moisture profiles by an ensemble Kalman filter: Effect of assimilation depth
1274 and frequency, 43, 2007.
- 1275 Ding, J., van der A, R. J., Mijling, B., Levelt, P. F., and Hao, N.: NO_x emission estimates during the
1276 2014 Youth Olympic Games in Nanjing, *Atmospheric Chemistry and Physics*, 15, 9399-9412,
1277 10.5194/acp-15-9399-2015, 2015.
- 1278 Elbern, H., Strunk, A., Schmidt, H., and Talagrand, O.: Emission rate and chemical state estimation

1279 by 4-dimensional variational inversion, *Atmospheric Chemistry and Physics*, 7, 3749-3769,
1280 10.5194/acp-7-3749-2007, 2007.

1281 Evensen, G.: The Ensemble Kalman Filter for Combined State and Parameter Estimation MONTE
1282 CARLO TECHNIQUES FOR DATA ASSIMILATION IN LARGE SYSTEMS, *Ieee Control*
1283 *Systems Magazine*, 29, 83-104, 10.1109/mcs.2009.932223, 2009.

1284 Feng, S., Jiang, F., Jiang, Z., Wang, H., Cai, Z., and Zhang, L.: Impact of 3DVAR assimilation of
1285 surface PM2.5 observations on PM2.5 forecasts over China during wintertime, *Atmospheric*
1286 *Environment*, 187, 34-49, 10.1016/j.atmosenv.2018.05.049, 2018.

1287 Feng, S., Jiang, F., Wang, H., Shen, Y., Zheng, Y., Zhang, L., Lou, C., and Ju, W.: Anthropogenic
1288 emissions estimated using surface observations and their impacts on PM2.5 source
1289 apportionment over the Yangtze River Delta, China, *Science of The Total Environment*, 828,
1290 154522, 2022

1291 Feng, S., Jiang, F., Wu, Z., Wang, H., Ju, W., and Wang, H.: CO Emissions Inferred From Surface
1292 CO Observations Over China in December 2013 and 2017, *Journal of Geophysical Research-*
1293 *Atmospheres*, 125, 10.1029/2019jd031808, 2020a.

1294 Feng, S., Jiang, F., Wang, H., Wang, H., Ju, W., Shen, Y., Zheng, Y., Wu, Z., and Ding, A.: NOx
1295 Emission Changes Over China During the COVID-19 Epidemic Inferred From Surface NO2
1296 Observations, *Geophysical Research Letters*, 47, 10.1029/2020gl090080, 2020b.

1297 Feng, S. and Jiang, F.: Anthropogenic air pollutant emissions over China inferred by Regional multi-
1298 Air Pollutant Assimilation System (RAPAS v1.0), Zenodo, 10.5281/zenodo.4718290, 2021.

1299 Gaspari, G. and Cohn, S. E.: Construction of correlation functions in two and three dimensions,
1300 *Quarterly Journal of the Royal Meteorological Society*, 125, 723-757, 10.1256/smsqj.55416,
1301 1999.

1302 Guenther, A. B., Jiang, X., Heald, C. L., Sakulyanontvittaya, T., Duhl, T., Emmons, L. K., and Wang,
1303 X.: The Model of Emissions of Gases and Aerosols from Nature version 2.1 (MEGAN2.1): an
1304 extended and updated framework for modeling biogenic emissions, *Geoscientific Model*
1305 *Development*, 5, 1471-1492, 10.5194/gmd-5-1471-2012, 2012.

1306 Gurney, K. R., Law, R. M., Denning, A. S., Rayner, P. J., Pak, B. C., Baker, D., Bousquet, P.,
1307 Bruhwiler, L., Chen, Y. H., Ciais, P., Fung, I. Y., Heimann, M., John, J., Maki, T., Maksyutov,
1308 S., Peylin, P., Prather, M., and Taguchi, S.: Transcom 3 inversion intercomparison: Model mean
1309 results for the estimation of seasonal carbon sources and sinks, *Global Biogeochemical Cycles*,
1310 18, 10.1029/2003gb002111, 2004.

1311 He, W., van der Velde, I. R., Andrews, A. E., Sweeney, C., Miller, J., Tans, P., van der Laan-Luijkx,
1312 I. T., Nehrkorn, T., Mountain, M., Ju, W., Peters, W., and Chen, H.: CTDAS-Lagrange v1.0: a
1313 high-resolution data assimilation system for regional carbon dioxide observations,
1314 *Geoscientific Model Development*, 11, 3515-3536, 10.5194/gmd-11-3515-2018, 2018.

1315 Hinds, W.C.: *Aerosol Technology: Properties, Behavior, and Measurement of Airborne Particles*.
1316 New York: John Wiley, 1982.

- 1317 Houtekamer, P. L. and Mitchell, H. L.: A sequential ensemble Kalman filter for atmospheric data
 1318 assimilation, *Monthly Weather Review*, 129, 123-137, 10.1175/1520-
 1319 0493(2001)129<0123:asekff>2.0.co;2, 2001.
- 1320 Houtekamer, P. L. and Zhang, F.: Review of the Ensemble Kalman Filter for Atmospheric Data
 1321 Assimilation, *Monthly Weather Review*, 144, 4489-4532, 10.1175/mwr-d-15-0440.1, 2016.
- 1322 Inness, A., Blechschmidt, A. M., Bouarar, I., Chabrilat, S., Crepulja, M., Engelen, R. J., Eskes, H.,
 1323 Flemming, J., Gaudel, A., Hendrick, F., Huijnen, V., Jones, L., Kapsomenakis, J., Katragkou,
 1324 E., Keppens, A., Langerock, B., de Maziere, M., Melas, D., Parrington, M., Peuch, V. H.,
 1325 Razinger, M., Richter, A., Schultz, M. G., Suttie, M., Thouret, V., Vrekoussis, M., Wagner, A.,
 1326 and Zerefos, C.: Data assimilation of satellite-retrieved ozone, carbon monoxide and nitrogen
 1327 dioxide with ECMWF's Composition-IFS, *Atmospheric Chemistry and Physics*, 15, 5275-5303,
 1328 2015.
- 1329 Jiang, F., Liu, Q., Huang, X., Wang, T., Zhuang, B., and Xie, M.: Regional modeling of secondary
 1330 organic aerosol over China using WRF/Chem, *Journal of Aerosol Science*, 43, 57-73,
 1331 10.1016/j.jaerosci.2011.09.003, 2012a.
- 1332 Jiang, F., Zhou, P., Liu, Q., Wang, T., Zhuang, B., and Wang, X.: Modeling tropospheric ozone
 1333 formation over East China in springtime, *Journal of Atmospheric Chemistry*, 69, 303-319,
 1334 10.1007/s10874-012-9244-3, 2012b.
- 1335 Jiang, F., Wang, H. M., Chen, J. M., Machida, T., Zhou, L. X., Ju, W. M., Matsueda, H., and Sawa,
 1336 Y.: Carbon balance of China constrained by CONTRAIL aircraft CO₂ measurements,
 1337 *Atmospheric Chemistry and Physics*, 14, 10133-10144, 10.5194/acp-14-10133-2014, 2014.
- 1338 Jiang, F., Wang, H., Chen, J. M., Ju, W., Tian, X., Feng, S., Li, G., Chen, Z., Zhang, S., Lu, X., Liu,
 1339 J., Wang, H., Wang, J., He, W., and Wu, M.: Regional CO₂ fluxes from 2010 to 2015 inferred
 1340 from GOSAT XCO₂ retrievals using a new version of the Global Carbon Assimilation System,
 1341 *Atmos. Chem. Phys.*, 21, 1963-1985, 10.5194/acp-21-1963-2021, 2021.
- 1342 Jiang, W., Smyth, S., Giroux, E., Roth, H., and Yin, D.: Differences between CMAQ fine mode
 1343 particle and PM_{2.5} concentrations and their impact on model performance evaluation in the
 1344 lower Fraser valley, *Atmospheric Environment*, 40, 4973-4985,
 1345 10.1016/j.atmosenv.2005.10.069, 2006.
- 1346 Jiang, Z., Jones, D. B. A., Worden, H. M., Deeter, M. N., Henze, D. K., Worden, J., Bowman, K. W.,
 1347 Brenninkmeijer, C. A. M., and Schuck, T. J.: Impact of model errors in convective transport on
 1348 CO source estimates inferred from MOPITT CO retrievals, *Journal Of Geophysical Research-
 1349 Atmospheres*, 118, 2073-2083, 2013a.
- 1350 Jiang, Z., Liu, Z., Wang, T., Schwartz, C. S., Lin, H.-C., and Jiang, F.: Probing into the impact of
 1351 3DVAR assimilation of surface PM₁₀ observations over China using process analysis, *Journal
 1352 of Geophysical Research: Atmospheres*, 118, 6738-6749, 10.1002/jgrd.50495, 2013b.
- 1353 Jiang, Z., Worden, J. R., Worden, H., Deeter, M., Jones, D. B. A., Arellano, A. F., and Henze, D. K.:
 1354 A 15-year record of CO emissions constrained by MOPITT CO observations, *Atmospheric
 1355 Chemistry And Physics*, 17, 4565-4583, 10.5194/acp-17-4565-2017, 2017.

- 1356 Jin, J., Lin, H. X., Heemink, A., and Segers, A.: Spatially varying parameter estimation for dust
 1357 emissions using reduced-tangent-linearization 4DVar, *Atmospheric Environment*, 187, 358-
 1358 373, 10.1016/j.atmosenv.2018.05.060, 2018.
- 1359 Kahnert, M.: Variational data analysis of aerosol species in a regional CTM: background error
 1360 covariance constraint and aerosol optical observation operators, *Tellus B*, 60, 2008.
- 1361 Kang, J.-S., Kalnay, E., Miyoshi, T., Liu, J., and Fung, I.: Estimation of surface carbon fluxes with
 1362 an advanced data assimilation methodology, 117, 10.1029/2012JD018259, 2012.
- 1363 Keppenne, C. L., Rienecker, M. M., Kurkowski, N. P., and Adamec, D. A.: Ensemble Kalman filter
 1364 assimilation of temperature and altimeter data with bias correction and application to seasonal
 1365 prediction, *Nonlin. Processes Geophys.*, 12, 491-503, 2005.
- 1366 Kleist, D. T., Parrish, D. F., Derber, J. C., Treadon, R., Wu, W.-S., and Lord, S.: Introduction of the
 1367 GSI into the NCEP Global Data Assimilation System, *Weather and Forecasting*, 24, 1691-1705,
 1368 10.1175/2009waf2222201.1, 2009.
- 1369 Kong, L., Tang, X., Zhu, J., Wang, Z., Pan, Y., Wu, H., Wu, L., Wu, Q., He, Y., Tian, S., Xie, Y., Liu,
 1370 Z., Sui, W., Han, L., and Carmichael, G.: Improved Inversion of Monthly Ammonia Emissions
 1371 in China Based on the Chinese Ammonia Monitoring Network and Ensemble Kalman Filter,
 1372 *Environmental Science & Technology*, 53, 12529-12538, 10.1021/acsest.9b02701, 2019a.
- 1373 Kong, L., Tang, X., Zhu, J., Wang, Z., Fu, J. S., Wang, X., Itahashi, S., Yamaji, K., Nagashima, T.,
 1374 Lee, H. J., Kim, C. H., Lin, C. Y., Chen, L., Zhang, M., Tao, Z., Li, J., Kajino, M., Liao, H.,
 1375 Sudo, K., Wang, Y., Pan, Y., Tang, G., Li, M., Wu, Q., Ge, B., and Carmichael, G. R.: Evaluation
 1376 and uncertainty investigation of the NO₂, CO and NH₃ modeling over China under the
 1377 framework of MICS-Asia III, *Atmos. Chem. Phys. Discuss.*, 2019, 1-33, 10.5194/acp-2018-
 1378 1158, 2019b.
- 1379 Laloyaux, P., Bonavita, M., Chrust, M., and Gürol, S.: Exploring the potential and limitations of
 1380 weak-constraint 4D-Var, *Quarterly Journal of the Royal Meteorological Society*, 146, 4067-
 1381 4082, 2020
- 1382 Li, J.-d., Deng, Q.-h., Lu, C., and Huang, B.-l.: Chemical compositions and source apportionment
 1383 of atmospheric PM₁₀ in suburban area of Changsha, China, *Journal of Central South
 1384 University of Technology*, 17, 509-515, 2010.
- 1385 Li, M., Zhang, Q., Kurokawa, J.-i., Woo, J.-H., He, K., Lu, Z., Ohara, T., Song, Y., Streets, D. G.,
 1386 Carmichael, G. R., Cheng, Y., Hong, C., Huo, H., Jiang, X., Kang, S., Liu, F., Su, H., and Zheng,
 1387 B.: MIX: a mosaic Asian anthropogenic emission inventory under the international
 1388 collaboration framework of the MICS-Asia and HTAP, *Atmospheric Chemistry and Physics*,
 1389 17, 935-963, 10.5194/acp-17-935-2017, 2017.
- 1390 Liu, C. and Shi, K.: A review on methodology in O₃-NO_x-VOC sensitivity study, *Environmental
 1391 Pollution*, 291, 118249, 2021.
- 1392 Liu, Y., Kalnay, E., Zeng, N., Asrar, G., Chen, Z., and Jia, B.: Estimating surface carbon fluxes based
 1393 on a local ensemble transform Kalman filter with a short assimilation window and a long
 1394 observation window: an observing system simulation experiment test in GEOS-Chem 10.1,

1395 Geoscientific Model Development, 12, 2899-2914, 2019.

1396 Liu, Z., Liu, Q., Lin, H.-C., Schwartz, C. S., Lee, Y.-H., and Wang, T.: Three-dimensional variational
 1397 assimilation of MODIS aerosol optical depth: Implementation and application to a dust storm
 1398 over East Asia, *Journal of Geophysical Research: Atmospheres*, 116, n/a-n/a,
 1399 10.1029/2011jd016159, 2011.

1400 Lorenc, A. C.: Modelling of error covariances by 4D-Var data assimilation, *Quarterly Journal of the*
 1401 *Royal Meteorological Society*, 129, 3167-3182, 2003.

1402 Hamer, P. D., Bowman, K. W., Henze, D. K., Attie, J. L., and Marecal, V.: The impact of observing
 1403 characteristics on the ability to predict ozone under varying polluted photochemical regimes,
 1404 *Atmospheric Chemistry and Physics*, 15, 10645-10667, 2015.

1405 Ma, C., Wang, T., Mizzi, A. P., Anderson, J. L., Zhuang, B., Xie, M., and Wu, R.: Multiconstituent
 1406 Data Assimilation With WRF-Chem/DART: Potential for Adjusting Anthropogenic Emissions
 1407 and Improving Air Quality Forecasts Over Eastern China, 124, 7393-7412,
 1408 10.1029/2019jd030421, 2019.

1409 Meirink, J. F., Bergamaschi, P., and Krol, M. C.: Four-dimensional variational data assimilation for
 1410 inverse modelling of atmospheric methane emissions: method and comparison with synthesis
 1411 inversion, *Atmospheric Chemistry and Physics*, 8, 6341-6353, 2008.

1412 Meirink, J. F., Eskes, H. J., and Goede, A. P. H.: Sensitivity analysis of methane emissions derived
 1413 from SCIAMACHY observations through inverse modelling, *Atmospheric Chemistry and*
 1414 *Physics*, 6, 1275-1292, 10.5194/acp-6-1275-2006, 2006.

1415 Maybeck: *Stochastic Models, Estimation and Control* Academic Press, 1979.

1416 Miyazaki, K. and Eskes, H.: Constraints on surface NO_x emissions by assimilating satellite
 1417 observations of multiple species, *Geophysical Research Letters*, 40, 4745-4750,
 1418 10.1002/grl.50894, 2013.

1419 Miyazaki, K., Eskes, H. J., and Sudo, K.: Global NO_x emission estimates derived from an
 1420 assimilation of OMI tropospheric NO₂ columns, *Atmospheric Chemistry and Physics*, 12,
 1421 2263-2288, 10.5194/acp-12-2263-2012, 2012a.

1422 Miyazaki, K., Eskes, H. J., Sudo, K., Takigawa, M., van Weele, M., and Boersma, K. F.:
 1423 Simultaneous assimilation of satellite NO₂, O₃, CO, and HNO₃ data for the analysis of
 1424 tropospheric chemical composition and emissions, *Atmospheric Chemistry and Physics*, 12,
 1425 9545-9579, 10.5194/acp-12-9545-2012, 2012b.

1426 Miyazaki, K., Eskes, H., Sudo, K., Boersma, K. F., Bowman, K., and Kanaya, Y.: Decadal changes
 1427 in global surface NO_x emissions from multi-constituent satellite data assimilation,
 1428 *Atmospheric Chemistry and Physics*, 17, 807-837, 2017.

1429 Mizzi, A. P., Edwards, D. P., and Anderson, J. L.: Assimilating compact phase space retrievals
 1430 (CPSRs): comparison with independent observations (MOZAIC in situ and IASI retrievals)
 1431 and extension to assimilation of truncated retrieval profiles, *Geoscientific Model Development*,
 1432 11, 3727-3745, 2018.

1433 Monteil, G., Houweling, S., Butz, A., Guerlet, S., Schepers, D., Hasekamp, O., Frankenberg, C.,
1434 Scheepmaker, R., Aben, I., and Rockmann, T.: Comparison of CH₄ inversions based on 15
1435 months of GOSAT and SCIAMACHY observations, *Journal of Geophysical Research-*
1436 *Atmospheres*, 118, 11807-11823, 2013.

1437 Muller, J. F. and Stavrakou, T.: Inversion of CO and NO_x emissions using the adjoint of the
1438 IMAGES model, *Atmospheric Chemistry and Physics*, 5, 1157-1186, 2005.

1439 Nassar, R., Jones, D. B. A., Kulawik, S. S., Worden, J. R., Bowman, K. W., Andres, R. J.,
1440 Suntharalingam, P., Chen, J. M., Brenninkmeijer, C. A. M., Schuck, T. J., Conway, T. J., and
1441 Worthy, D. E.: Inverse modeling of CO₂ sources and sinks using satellite observations of CO₂
1442 from TES and surface flask measurements, *Atmospheric Chemistry and Physics*, 11, 6029-
1443 6047, 2011.

1444 Navon, I. M.: Practical and theoretical aspects of adjoint parameter estimation and identifiability in
1445 meteorology and oceanography, *Dynamics of Atmospheres and Oceans*, 27, 55-79, 1998.

1446 Parrish, D. F. and Derber, J. C.: The National Meteorological Center's spectral statistical-
1447 interpolation analysis system, *Monthly Weather Review*, 120, 1747-1763, 10.1175/1520-
1448 0493(1992)120<1747:tnmcss>2.0.co;2, 1992.

1449 Paulot, F., Jacob, D. J., Pinder, R. W., Bash, J. O., Travis, K., and Henze, D. K.: Ammonia emissions
1450 in the United States, European Union, and China derived by high-resolution inversion of
1451 ammonium wet deposition data: Interpretation with a new agricultural emissions inventory
1452 (MASAGE_NH₃), *Journal of Geophysical Research-Atmospheres*, 119, 4343-4364, 2014.

1453 Peng, Z., Liu, Z., Chen, D., and Ban, J.: Improving PM_{2.5} forecast over
1454 China by the joint adjustment of initial conditions and source emissions with an ensemble
1455 Kalman filter, *Atmospheric Chemistry and Physics*, 17, 4837-4855, 10.5194/acp-17-4837-
1456 2017, 2017.

1457 Peng, Z., Lei, L., Liu, Z., Su, J., Ding, A., Ban, J., Chen, D., Kou, X., and Chu, K.: The impact of
1458 multi-species surface chemical observation assimilation on air quality forecasts in China,
1459 *Atmospheric Chemistry and Physics*, 18, 10.5194/acp-18-17387-2018, 2018.

1460 Peters, W., Jacobson, A. R., Sweeney, C., Andrews, A. E., Conway, T. J., Masarie, K., Miller, J. B.,
1461 Bruhwiler, L. M. P., Petron, G., Hirsch, A. I., Worthy, D. E. J., van der Werf, G. R., Randerson,
1462 J. T., Wennberg, P. O., Krol, M. C., and Tans, P. P.: An atmospheric perspective on North
1463 American carbon dioxide exchange: CarbonTracker, *Proceedings of the National Academy of*
1464 *Sciences of the United States of America*, 104, 18925-18930, 10.1073/pnas.0708986104, 2007.

1465 Peylin, P., Rayner, P. J., Bousquet, P., Carouge, C., Hourdin, F., Heinrich, P., Ciais, P., and
1466 contributors, A.: Daily CO₂ flux estimates over Europe from continuous atmospheric
1467 measurements: 1, inverse methodology, *Atmospheric Chemistry and Physics*, 5, 3173-3186,
1468 10.5194/acp-5-3173-2005, 2005.

1469 Purser, R. J., Wu, W. S., Parrish, D. F., and Roberts, N. M.: Numerical aspects of the application of
1470 recursive filters to variational statistical analysis. Part I: Spatially homogeneous and isotropic
1471 Gaussian covariances, *Monthly Weather Review*, 131, 1524-1535, 10.1175//1520-

1472 0493(2003)131<1524:naotao>2.0.co;2, 2003.

1473 Quan, J., Liu, Q., Li, X., Gao, Y., Jia, X., Sheng, J., Liu, Y., 2015. Effect of heterogeneous aqueous
1474 reactions on the secondary formation of inorganic aerosols during haze events. *Atmospheric*
1475 *Environment* 122, 306-312.

1476 Rabier, F., McNally, A., Andersson, E., Courtier, P., Uden, P., Eyre, J., Hollingsworth, A., and
1477 Bouttier, F.: The ECMWF implementation of three-dimensional variational assimilation (3D-
1478 Var). II: Structure functions, *Quarterly Journal Of the Royal Meteorological Society*, 124,
1479 1809-1829, 10.1256/smsqj.55002, 1998.

1480 Reichle, R. H., McLaughlin, D. B., and Entekhabi, D.: Hydrologic data assimilation with the
1481 ensemble Kalman filter, *Monthly Weather Review*, 130, 103-114, 2002.

1482 Richardson, H., Basu, S., and Holtslag, A. A. M.: Improving Stable Boundary-Layer Height
1483 Estimation Using a Stability-Dependent Critical Bulk Richardson Number, *Boundary-Layer*
1484 *Meteorology*, 148, 93-109, 2013.

1485 Ruiz, J. and Pulido, M.: Parameter Estimation Using Ensemble-Based Data Assimilation in the
1486 Presence of Model Error, *Monthly Weather Review*, 143, 1568-1582, 2015.

1487 Sarwar, G., Simon, H., Bhave, P., and Yarwood, G.: Examining the impact of heterogeneous nitril
1488 chloride production on air quality across the United States, *Atmospheric Chemistry and*
1489 *Physics*, 12, 6455-6473, 10.5194/acp-12-6455-2012, 2012.

1490 Sasaki, Y.: SOME BASIC FORMALISMS IN NUMERICAL VARIATIONAL ANALYSIS,
1491 *Monthly Weather Review*, 98, 875-&, 1970.

1492 Schneising, O., Buchwitz, M., Burrows, J. P., Bovensmann, H., Bergamaschi, P., and Peters, W.:
1493 Three years of greenhouse gas column-averaged dry air mole fractions retrieved from satellite
1494 - Part 2: Methane, *Atmospheric Chemistry and Physics*, 9, 443-465, 2009.

1495 Schwartz, C. S., Liu, Z., Lin, H.-C., and Cetola, J. D.: Assimilating aerosol observations with a
1496 "hybrid" variational-ensemble data assimilation system, *Journal Of Geophysical Research-*
1497 *Atmospheres*, 119, 4043-4069, 10.1002/2013jd020937, 2014.

1498 Sekiyama, T. T., Tanaka, T. Y., Shimizu, A., and Miyoshi, T.: Data assimilation of CALIPSO aerosol
1499 observations, *Atmospheric Chemistry and Physics*, 10, 39-49, 10.5194/acp-10-39-2010, 2010.

1500 Shen, Y., Jiang, F., Feng, S., Zheng, Y., Cai, Z., and Lyu, X.: Impact of weather and emission changes
1501 on NO₂ concentrations in China during 2014–2019, *Environmental Pollution*, 269, 116163,
1502 10.1016/j.envpol.2020.116163, 2021.

1503 Shi, X. and Brasseur, G. P.: The Response in Air Quality to the Reduction of Chinese Economic
1504 Activities During the COVID-19 Outbreak, 47, e2020GL088070, 10.1029/2020gl088070,
1505 2020.

1506 Stanevich, I., Jones, D. B. A., Strong, K., Keller, M., Henze, D. K., Parker, R. J., Boesch, H., Wunch,
1507 D., Notholt, J., Petri, C., Warneke, T., Sussmann, R., Schneider, M., Hase, F., Kivi, R.,
1508 Deutscher, N. M., Velasco, V. A., Walker, K. A., and Deng, F.: Characterizing model errors in
1509 chemical transport modeling of methane: using GOSAT XCH₄ data with weak-constraint four-

1510 dimensional variational data assimilation, *Atmospheric Chemistry and Physics*, 21, 9545-9572,
1511 2021.

1512 Stavrakou, T., Müller, J.-F., Boersma, K. F., De Smedt, I., and van der A, R. J.: Assessing the
1513 distribution and growth rates of NO_x emission sources by inverting a 10-year record of NO₂
1514 satellite columns, 35, 10.1029/2008gl033521, 2008.

1515 Sun, A. Y., Morris, A., and Mohanty, S.: Comparison of deterministic ensemble Kalman filters for
1516 assimilating hydrogeological data, *Advances in Water Resources*, 32, 280-292,
1517 10.1016/j.advwatres.2008.11.006, 2009.

1518 Takagi, H., Saeki, T., Oda, T., Saito, M., Valsala, V., Belikov, D., Saito, R., Yoshida, Y., Morino, I.,
1519 Uchino, O., Andres, R. J., Yokota, T., and Maksyutov, S.: On the Benefit of GOSAT
1520 Observations to the Estimation of Regional CO₂ Fluxes, *SOLA*, 7, 161-164,
1521 10.2151/sola.2011-041, 2011.

1522 Tang, X., Zhu, J., Wang, Z. F., and Gbaguidi, A.: Improvement of ozone forecast over Beijing based
1523 on ensemble Kalman filter with simultaneous adjustment of initial conditions and emissions,
1524 *Atmospheric Chemistry And Physics*, 11, 12901-12916, 10.5194/acp-11-12901-2011, 2011.

1525 Tang, X., Zhu, J., Wang, Z. F., Wang, M., Gbaguidi, A., Li, J., Shao, M., Tang, G. Q., and Ji, D. S.:
1526 Inversion of CO emissions over Beijing and its surrounding areas with ensemble Kalman filter,
1527 *Atmospheric Environment*, 81, 676-686, 10.1016/j.atmosenv.2013.08.051, 2013.

1528 Wang, C., Lei, L., Tan, Z.-M., and Chu, K.: Adaptive Localization for Tropical Cyclones With
1529 Satellite Radiances in an Ensemble Kalman Filter, *Frontiers in Earth Science*, 8,
1530 10.3389/feart.2020.00039, 2020.

1531 Wang, H., Jiang, F., Wang, J., Ju, W., and Chen, J. M.: Terrestrial ecosystem carbon flux estimated
1532 using GOSAT and OCO-2 XCO₂ retrievals, *Atmospheric Chemistry and Physics*, 19, 12067-
1533 12082, 2019a.

1534 Wang, N., Lyu, X., Deng, X., Huang, X., Jiang, F., and Ding, A.: Aggravating O₃ pollution due to
1535 NO_x emission control in eastern China, *Science of The Total Environment*, 677, 732-744,
1536 2019b.

1537 Wang, Y. H., Hu, B., Ji, D. S., Liu, Z. R., Tang, G. Q., Xin, J. Y., Zhang, H. X., Song, T., Wang, L.
1538 L., Gao, W. K., Wang, X. K., and Wang, Y. S.: Ozone weekend effects in the Beijing-Tianjin-
1539 Hebei metropolitan area, China, *Atmospheric Chemistry and Physics*, 14, 2419-2429, 2014.

1540 Wang, Z., Li, Y., Dong, X., Sun, R., Sun, N., and Pan, L.: Analysis on weekend effect of air
1541 pollutants in urban atmosphere of Beijing, *Journal of University of Chinese Academy of
1542 Sciences*, 32, 843-850, 2015.

1543 Wang, Z., Wang, W., Tham, Y.J., Li, Q., Wang, H., Wen, L., Wang, X., Wang, T., 2017. Fast
1544 heterogeneous N₂O₅ uptake and ClNO₂ production in power plant and industrial plumes
1545 observed in the nocturnal residual layer over the North China Plain. *Atmospheric Chemistry
1546 and Physics* 17, 12361-12378.

1547 Wecht, K. J., Jacob, D. J., Sulprizio, M. P., Santoni, G. W., Wofsy, S. C., Parker, R., Boesch, H., and

1548 Worden, J.: Spatially resolving methane emissions in California: constraints from the CalNex
1549 aircraft campaign and from present (GOSAT, TES) and future (TROPOMI, geostationary)
1550 satellite observations, *Atmospheric Chemistry and Physics*, 14, 8173-8184, 2014.

1551 Wu, H., Tang, X., Wang, Z., Wu, L., Li, J., Wang, W., Yang, W., and Zhu, J.: High-spatiotemporal-
1552 resolution inverse estimation of CO and NO_x emission reductions during emission control
1553 periods with a modified ensemble Kalman filter, *Atmospheric Environment*, 236,
1554 10.1016/j.atmosenv.2020.117631, 2020.

1555 Wu, W. S., Purser, R. J., and Parrish, D. F.: Three-dimensional variational analysis with spatially
1556 inhomogeneous covariances, *Monthly Weather Review*, 130, 2905-2916, 10.1175/1520-
1557 0493(2002)130<2905:tdvaws>2.0.co;2, 2002.

1558 Yang, W., Li, J., Wang, W., Li, J., Ge, M., Sun, Y., Chen, X., Ge, B., Tong, S., Wang, Q., and Wang,
1559 Z.: Investigating secondary organic aerosol formation pathways in China during 2014,
1560 *Atmospheric Environment*, 213, 133-147, 2019.

1561 Yumimoto, K., Uno, I., Sugimoto, N., Shimizu, A., Liu, Z., and Winker, D. M.: Adjoint inversion
1562 modeling of Asian dust emission using lidar observations, *Atmospheric Chemistry and Physics*,
1563 8, 2869-2884, 2008.

1564 Zhang, F., Weng, Y., Sippel, J. A., Meng, Z., and Bishop, C. H.: Cloud-Resolving Hurricane
1565 Initialization and Prediction through Assimilation of Doppler Radar Observations with an
1566 Ensemble Kalman Filter, *Monthly Weather Review*, 137, 2105-2125, 10.1175/2009mwr2645.1,
1567 2009a.

1568 Zhang, L., Chen, Y., Zhao, Y., Henze, D. K., Zhu, L., Song, Y., Paulot, F., Liu, X., Pan, Y., Lin, Y.,
1569 and Huang, B.: Agricultural ammonia emissions in China: reconciling bottom-up and top-down
1570 estimates, *Atmospheric Chemistry and Physics*, 18, 339-355, 2018.

1571 Zhang, Q., Streets, D. G., Carmichael, G. R., He, K. B., Huo, H., Kannari, A., Klimont, Z., Park, I.
1572 S., Reddy, S., Fu, J. S., Chen, D., Duan, L., Lei, Y., Wang, L. T., and Yao, Z. L.: Asian emissions
1573 in 2006 for the NASA INTEX-B mission, *Atmospheric Chemistry and Physics*, 9, 5131-5153,
1574 10.5194/acp-9-5131-2009, 2009b.

1575 Zhang, S., Zheng, X., Chen, J. M., Chen, Z., Dan, B., Yi, X., Wang, L., and Wu, G.: A global carbon
1576 assimilation system using a modified ensemble Kalman filter, *Geosci. Model Dev.*, 8, 805-816,
1577 10.5194/gmd-8-805-2015, 2015.

1578 Zhang, X., Liu, J., Han, H., Zhang, Y., Jiang, Z., Wang, H., Meng, L., Li, Y. C., and Liu, Y.: Satellite-
1579 Observed Variations and Trends in Carbon Monoxide over Asia and Their Sensitivities to
1580 Biomass Burning, *Remote Sensing*, 12, 10.3390/rs12050830, 2020.

1581 Zheng, B., Tong, D., Li, M., Liu, F., Hong, C., Geng, G., Li, H., Li, X., Peng, L., Qi, J., Yan, L.,
1582 Zhang, Y., Zhao, H., Zheng, Y., He, K., and Zhang, Q.: Trends in China's anthropogenic
1583 emissions since 2010 as the consequence of clean air actions, *Atmospheric Chemistry And
1584 Physics*, 18, 14095-14111, 10.5194/acp-18-14095-2018, 2018.

1585 Zheng, B., Zhang, Q., Tong, D., Chen, C., Hong, C., Li, M., Geng, G., Lei, Y., Huo, H., and He, K.:
1586 Resolution dependence of uncertainties in gridded emission inventories: a case study in Hebei,

